RSC Advances

PAPER

View Article Online
View Journal | View Issue

Cite this: *RSC Adv.*, 2026, **16**, 29950

Polysaccharide-stabilized biogenic CuO/SeO_2 nanocomposites: green synthesis, physicochemical characterization, and enhanced antioxidant, antimicrobial, and selective anticancer activities

Khaled M. Elattar, *[a] Ashraf Elsayed,[b] Alaa Elmetwalli,[c] Mohammed S. El-Hersh,[d] Ayman El-Khateeb,[e] Ahmed A. Zaher,[f] Nesma M. Bayoumy,[g] Mohamed Abdel Salam,[h] Khalid M. Ghoneem[i] and Abdulaziz A. Al-Askar*[j]

A green-assisted synthesis route was employed for the preparation of copper oxide/selenium dioxide (CuO/SeO_2) and their polysaccharide-functionalized counterpart (CuO/SeO_2/polysaccharide NCs), using clove extract as a reducing, chelating, and stabilizing agent. The formation of a crystalline CuO/SeO_2 framework was confirmed through comprehensive characterization using X-ray photoelectron spectroscopy (XPS), X-ray diffraction (XRD), ultraviolet-visible spectroscopy (UV-Vis), Fourier-transform infrared spectroscopy (FTIR), high-resolution transmission electron microscopy (HR-TEM), scanning electron microscopy (SEM), energy-dispersive X-ray spectroscopy (EDX), and zeta potential analysis, while a core–shell-like hybrid structure was suggested based on morphological observations. Phytochemical analysis revealed a reduction in phenolic compounds during the nanoparticle formation process, whereas an appreciable increase was observed in carbohydrates after the addition of the polysaccharide. The CuO/SeO_2/polysaccharide NC exhibited enhanced antioxidant activity, with a DPPH IC_{50} value of 0.0096 ± 0.001 mg mL^{-1}. Antibacterial activity exhibited strong, species-dependent inhibition, reaching a maximum of 38 ± 0.08 mm against *Klebsiella pneumoniae* with enhanced activity observed particularly against Gram-positive bacteria. Notably, the results obtained from the cytotoxicity assays demonstrated selective anticancer activity with low cytotoxicity against WI-38 normal fibroblasts (IC_{50} = 328.2 μg mL^{-1}) and significant inhibitory effects against cancer cell lines, PC3 (IC_{50} = 18.42 μg mL^{-1}), HeLa (13.70 μg mL^{-1}), HT-29 (13.03 μg mL^{-1}), and A549 (14.14 μg mL^{-1}). The results demonstrate that polysaccharide-functionalized CuO/SeO_2 nanocomposites exhibit enhanced physicochemical stability and tunable biological properties, highlighting their potential for further investigation in antioxidant, antimicrobial, and anticancer applications.

Received 21st January 2026
Accepted 23rd May 2026

DOI: 10.1039/d6ra00556j

rsc.li/rsc-advances

1 Introduction

The global transition to sustainable technologies has accelerated the development of green nanotechnology, driven by the need to replace hazardous chemical processes with energy-efficient and environmentally benign alternatives. Green synthesis routes to nanomaterials have attracted significant attention due to the elimination of toxic reagents, reduced cost, and scalability, clearly demonstrated in numerous studies, including the pioneering work of Cao *et al.*[1] Such eco-friendly

[a]*Unit of Genetic Engineering and Biotechnology, Mansoura University, El-Gomhoria St., Mansoura, 35516, Egypt. E-mail: khaledelattar2@yahoo.com; khaledelattar2@mans.edu.eg*

[b]*Botany Department, Faculty of Science, Mansoura University, Mansoura 35516, Egypt. E-mail: ashraf-badawy@mans.edu.eg*

[c]*Prince Fahad bin Sultan Research Chair for Biomedical Research, University of Tabuk, Tabuk, Saudi Arabia. E-mail: dr.prof2011@gmail.com; aelmetwalli@ut.edu.sa*

[d]*Microbial Activity Unit, Department of Microbiology, Soils, Water and Environment Research Institute, Agricultural Research Center, Giza, 12619, Egypt. E-mail: m.elhersh@yahoo.com*

[e]*Department of Agricultural Chemistry, Faculty of Agriculture, Mansoura University, Mansoura, 35516, Egypt. E-mail: aymanco@mans.edu.eg*

[f]*Chemistry Department, Faculty of Science, Mansoura University, Mansoura 35516, Egypt. E-mail: smart.zaher@yahoo.com*

[g]*Dental Biomaterials Department, Faculty of Oral and Dental Medicine, Delta University for Science and Technology, Gamasa, Egypt. E-mail: nesma.bayoumy@deltauniv.edu.eg*

[h]*Department of Chemistry, College of Science and Technology, Florida A&M University, 1530 S. Martin Luther King Blvd, Jones Hall 219, Tallahassee, Florida 32307, USA. E-mail: mohamed.salam@famu.edu*

[i]*Department of Seed Pathology Research, Plant Pathology Research Institute, Agricultural Research Center (ARC), Giza 12619, Egypt. E-mail: khalidghoneem@arc.sci.eg*

[j]*Botany and Microbiology Department, Faculty of Science, King Saud University, Riyadh 11451, Saudi Arabia. E-mail: aalaskara@ksu.edu.sa; Tel: +201010655354*

methodologies are in agreement with modern principles of circular chemistry and enable the synthesis of various classes of nanomaterials such as metal, metal oxide, ceramic, polymeric, and carbon-based nanoparticles, all with tunable physicochemical properties relevant to biomedical, catalytic, sensing, and environmental applications.[2,3]

The biomedical potential of nanoscale systems is largely attributed to their high surface-to-volume ratios, improved reactivity, and modifiable surface chemistry, which are critical for addressing major global health challenges such as antimicrobial resistance. As remarked by Dhingra *et al.*,[4] antimicrobial resistance (AMR) has emerged as a major global public health concern, resulting in catastrophic treatment failures and increased morbidity and mortality burdens worldwide. This rapid emergence and spread of multidrug-resistant (MDR) pathogens are partially attributed to the improper use of antibiotics, genetic adaptability, and the formation of biofilms. There is now an immediate need to discover novel types of antimicrobial platforms that can avoid conventional resistance mechanisms.[5] Various metal nanoparticles like Ag_2O, ZnO, Au, TiO_2, CuO, and ZrO_2 have also been shown to have broad-spectrum antibacterial properties against various clinical isolates like *E. coli*, *K. pneumoniae*, and *P. aeruginosa* in the past, as shown in various publications.[6,7]

On the other hand, nanomaterials have displayed growing interest in the oncology field for their potential to trigger apoptosis, regulate reduction pathways, and resist drug resistance, enabling more effective targeted drug delivery. Despite this, cancer is still one of the leading causes of death worldwide, accounting for over 10 million deaths annually, and conventional therapies, such as surgery, radiotherapy, chemotherapy, immunotherapy, and hormonal therapy, are limited by systemic toxicity, poor selectivity, and rapid resistance development.[8] These shortfalls have given rise to nanotechnology-based anticancer systems, among which are bimetallic nanostructures, polymeric carriers, hybrid nanocomposites, and advanced delivery platforms.[9]

Among several developing nanosystems, selenium nanostructures have attracted considerable attention owing to their unique biological and therapeutic properties. Selenium is an important trace metal that plays a role in various antioxidant enzymes like glutathione peroxidase and thioredoxin reductase; hence, it plays key roles in redox balance, immune regulation, and cytoprotection.[10] Biogenic selenium nanoparticles (SeNPs) have demonstrated significant anticancer and antioxidant properties in many studies due to mechanisms that involve mitochondrial depolarization, caspase-9 activation, and p53-dependent apoptosis.[11] Green synthesis of SeNPs has special advantages because phytochemicals like phenolics, flavonoids, proteins, and polysaccharides act as natural reducing, stabilizing, and functionalizing agents for SeNPs.[12] This has opened the avenue for using various botanical extracts such as tea, onion, ginger, and related herbs for efficient reduction of selenite ions into stable nanosystems.[13]

Within this context, copper-based nanomaterials represent another important class of bioactive nanostructures with outstanding catalytic, electrical, optical, and biological properties. Especially, CuO nanoparticles have demonstrated strong antimicrobial, antioxidant, and anticancer activities, thus justifying their use in medicine, agriculture, catalysis, and biosensing.[14] However, it is repeatedly pointed out in several reports that bimetallic and hybrid nanostructures often exhibit higher performance compared to their monometallic counterparts due to the effects of synergistic interactions, increased stability, and improved reactivity.[15] Indeed, systems such as Ag/Au, ZnO/CuO, Ag/Au-starch hybrids, and other biofabricated bimetallic composites have exhibited superior antimicrobial and anticancer efficacy compared to their individual components.[16] Despite the tremendous growth of green nanotechnology, biological activities, stability, and polysaccharide-mediated functionalization of biogenic bimetallic CuO/SeO_2 nanocomposites are still almost unexplored. Polysaccharides act as excellent bio-stabilizers, biocompatible capping agents, and often enhance aqueous stability, reduce aggregation, improve cellular uptake, translating into improved therapeutic performance.

Herein, this work reports the green biosynthesis of novel CuO/SeO_2 nanocomposites using *Syzygium aromaticum* (clove) extract and subsequently their surface functionalization with propolis-derived polysaccharides. The resultant nanocomposites were characterized comprehensively by Fourier-transform infrared spectroscopy (FTIR), ultraviolet-visible spectroscopy (UV-Vis), X-ray diffraction (XRD), X-ray photoelectron spectroscopy (XPS), transmission electron microscopy (TEM), scanning electron microscopy (SEM), energy-dispersive X-ray spectroscopy (EDX), and elemental mapping. Besides determining the antioxidant capacity of biosynthesized nanomaterials, their biological performance has been further modulated *via* polysaccharide coating. Both native and polysaccharide-stabilized CuO/SeO_2 nanocomposites have been assessed for anticancer and antimicrobial activities. This integrative green-assisted approach provides a potentially scalable and biologically effective strategy to engineer functional bimetallic nanostructures with tremendous therapeutic applications.

2 Materials and methods

2.1. Reagents and chemicals

Raw propolis samples were obtained from a certified local apiary and stored at 4 °C before use. Dried clove buds (*Syzygium aromaticum*) were purchased from a local herbal market, authenticated botanically, washed, air-dried, and finely powdered before extraction. Copper sulfate pentahydrate ($CuSO_4 \cdot 5H_2O$, ≥99.0%), selenium dioxide (SeO_2, ≥99.5%), gallic acid (≥98.0%), quercetin (≥98.0%), catechin (≥98.0%), glucose (≥99.5%), Folin–Ciocalteu reagent, aluminum chloride hexahydrate ($AlCl_3 \cdot 6H_2O$, ≥99.0%), vanillin (≥99.0%), anthrone (≥99.0%), 2,2-diphenyl-1-picrylhydrazyl (DPPH, ≥95.0%), ammonium molybdate tetrahydrate (≥99.0%), sodium phosphate monobasic (≥99.0%), potassium ferricyanide (≥99.0%), ferric chloride hexahydrate (≥99.0%), trichloroacetic acid (≥99.0%), and sodium carbonate (≥99.5%) were all obtained from Sigma-Aldrich (St. Louis, MO, USA). For more details of chemicals and reagents, see SI (Section S1).

2.2. Instruments

All characterizations were performed using standard analytical techniques. UV-Vis spectra were recorded on a Spekol 11 spectrophotometer (Analytik Jena, Germany), while functional groups were identified by FTIR (Thermo Scientific Nicolet IS10, USA). Morphology and elemental composition were analyzed by FE-SEM (JEOL JSM-7610F, Japan) coupled with EDX and elemental mapping (Oxford X-Max 80, UK), and internal structure was examined by HR-TEM (Thermo Scientific Talos F200i, USA). Crystalline phases were determined by XRD (PANalytical Philips, Netherlands) using Cu Kα radiation, and surface chemical states were analyzed by XPS (Thermo Scientific K-Alpha+, USA). Colloidal stability was assessed by zeta potential analysis (HORIBA SZ-100, Japan), performed on freshly prepared colloidal suspensions in distilled water prior to centrifugation under near-neutral conditions (pH ≈ 6.5–7.0). Sonication (Elma Schmidbauer GmbH, Germany), centrifugation (Beckman Coulter Allegra X-15R, USA), and a Memmert WB14 water bath shaker (Germany) were used during synthesis and extraction (Section S1).

2.3. Extraction of polysaccharides from propolis

Polysaccharides in the raw propolis samples were obtained by using the reported method with a slight modification.[17] Purified, powdered, 95% ethanol-defatted, and air-dried samples of propolis were used. Then, the defatted powder was dissolved in water. The solution underwent hot water extraction at 80–90 °C for 2 h, followed by centrifugation to remove the insoluble parts. The solution was concentrated by heating, and polysaccharides were obtained by ethanol precipitation, washed, and dried. Proteins were removed by Sevag deproteinization and dialyzed against deionized water for 48 h. The purified polysaccharides were then lyophilized into a dry powder that could be preserved at −20 °C.

2.4. Extraction of clove (*Syzygium aromaticum*)

The bioactive compounds present in the clove were extracted using ethanol (70%). The extract serves as a source of bioactive compounds and acts as a reducing and stabilizing agent during nanocomposite formation. The clove powder (10 g) was carefully weighed using the lab balance. This powder was added to the 250 mL Erlenmeyer flask. The 70% ethanol (v/v) solution was prepared by adding 70 mL of absolute ethanol to 30 mL of distilled water. A 100 mL solution was added to the clove powder sample. The suspension was stirred for 6 h in a temperature range of 25 ± 2 °C for the efficient dissolution of the bioactive compounds, such as polyphenols, flavonoids, and other compounds present in the clove. The mixture was filtered using Whatman No. 1 filter paper to remove insoluble residues. The filtered solution was then collected and stored in the amber-colored container at 4 °C.

2.5. Green synthesis of nanocomposites

2.5.1. Synthesis of CuO/SeO_2 nanocomposite. The CuO/SeO_2 nanocomposite was prepared through a green-chemistry method using clove (*Syzygium aromaticum*) extract as a reducing and stabilizing agent. Briefly, 50 mL of freshly prepared clove extracts (8.45 mg mL^{-1}) were heated to 45 °C under gentle stirring. In another beaker, 0.5 g of copper sulfate pentahydrate ($CuSO_4 \cdot 5H_2O$) was dissolved in 25 mL of distilled water, and 0.25 g of selenium dioxide (SeO_2) was separately dissolved in 25 mL of distilled water. The $CuSO_4$ solution was added dropwise to the clove extracts under continuous stirring, followed by the slow dripping of the SeO_2 solution. The reaction mixture was maintained at 45 °C with gentle stirring for 3 hours. Thereafter, sonication of the resulting suspension of CuO/SeO_2 NC was carried out at 60 °C for 3 hours to improve the dispersion and nucleation of particles. The solid CuO/SeO_2 NC was collected through centrifugation under 10 000×*g* forces for 15 min, thrice washed with 70% ethanol to remove excess precursors and phytocontents, and finally dried under vacuum at 50 °C.[18]

2.5.2. Preparation of CuO/SeO_2/polysaccharide nanocomposite. The CuO/SeO_2/polysaccharide-functionalized nanocomposite was synthesized similarly, and propolis-derived polysaccharide was included for improved stability and specificity. To begin with, a combination of 50 mL of clove extract, which was 8.45 mg mL^{-1}, and 0.2 g of propolis polysaccharide was dissolved in distilled water and heated to 45 °C under stirring for a homogenous solution to be attained. Copper sulfate, which consisted of 0.5 g in 25 mL of distilled water, and selenium dioxide, which consisted of 0.25 g in 25 mL of distilled water, were prepared separately and subsequently added to the clove-polysaccharide blend under continuous stirring. This was further kept under stirring and a temperature of 45 °C for 3 h for thorough formation of the CuO/SeO_2 polysaccharide-functionalized nanocomposite. This was further subjected to sonication for 4 h and a temperature of 60 °C for thorough particle dispersal and successful surface modification. The finalized CuO/SeO_2/polysaccharide NC was further separated through centrifugation at 10 000×*g* for 15 min, and further purification was done thrice with 70% ethanol. It was then desiccated under vacuum at 50 °C.[19] The synthesis process proceeded under mild reaction conditions and involved plant-derived reagents, which may reduce the use of hazardous chemicals compared to conventional chemical routes. Although it is difficult to calculate the atom economy and *E*-factor accurately due to the composition of the plant extract, this process is considered to have low energy input and a reduced environmental impact compared to conventional chemical synthesis. However, more optimization is still required to validate the sustainability of this process.

2.6. Phytochemical analyses

2.6.1. Determination of total phenolic content. Total phenolic content (TPC) was determined using the Folin–Ciocalteu colorimetric method with gallic acid as the reference standard.[20] Briefly, an aliquot of the sample was mixed with Folin–Ciocalteu reagent previously diluted with distilled water. After an initial incubation period, sodium carbonate solution (7.5%, w/v) was added to the mixture, which was then incubated

at room temperature in the dark for 30 min. The absorbance was measured at 765 nm using a UV-Vis spectrophotometer. A calibration curve was constructed using gallic acid solutions of known concentrations, and TPC was calculated from the regression equation and expressed as mg gallic acid equivalents (GAE).

2.6.2. Determination of total flavonoid content. Total flavonoid content (TFC) was quantified using the aluminum chloride colorimetric method, employing quercetin as the standard compound.[21] In brief, a measured volume of sample was mixed with aluminum chloride solution (2%, w/v) and potassium acetate solution, followed by dilution with distilled water. The reaction mixture was incubated at room temperature for 30 min to allow complex formation between flavonoids and aluminum ions. Absorbance was recorded at 415 nm against a reagent blank. Flavonoid content was calculated from a quercetin calibration curve and expressed as mg quercetin equivalents (QE).

2.6.3. Determination of tannin content. Condensed tannin content was determined using the vanillin–hydrochloric acid assay with catechin as the reference standard.[22] Briefly, the sample was mixed with freshly prepared vanillin reagent (1%, w/v vanillin in methanol), followed by the addition of concentrated hydrochloric acid. The reaction mixture was incubated at room temperature for 20 min to allow color development. Absorbance was measured at 500 nm using a UV-Vis spectrophotometer. A catechin standard curve was used for quantification, and tannin content was expressed as mg catechin equivalents (CE).

2.6.4. Anthrone assay. Total carbohydrate levels were quantified using the anthrone-based colorimetric assay, employing glucose as the calibration standard.[23] In brief, a measured volume of each sample was reacted with freshly prepared anthrone reagent (0.2% w/v anthrone dissolved in concentrated sulfuric acid). The reaction mixtures were heated in a boiling water bath for 10 min, then immediately cooled to ambient temperature. Absorbance was recorded at 620 nm using a UV-Vis spectrophotometer. A glucose standard curve was generated ($y = 0.0041x$; $R^2 = 0.9605$), and carbohydrate content was calculated from the corresponding regression equation and reported as mg glucose equivalents (GE).

2.7. Antioxidant activity

2.7.1. DPPH assay. Antioxidant properties of the synthesized nanocomposites and clove extract were measured using the DPPH radical scavenging assay.[24] DPPH solution of concentration 0.1 mM is freshly prepared using methanol. Stock solutions of the sample were mixed with an equal amount of DPPH solution at a ratio of 1 : 1 (v/v). This mixture is allowed to stand at room temperature for a period of 30 min in the dark. Reducing absorbance values were measured using a UV-Vis Spectrophotometer at a wavelength of 517 nm. Radical scavenging efficiency (%) is calculated using the following formula (eqn (1)):

$$\text{Scavenging activity } (\%) = \frac{(A_{\text{control}} - A_{\text{sample}})}{A_{\text{control}}} \times 100 \quad (1)$$

where A_{control} is the absorbance of the DPPH radical solution in the absence of the tested sample (DPPH + methanol), and A_{sample} is the absorbance of the tested sample. Ascorbic acid was taken as the positive control. The IC_{50} values, the concentration necessary to produce 50% inhibition of the DPPH radicals, were determined from the graph drawn by taking the % inhibition of DPPH values on the *Y*-axis against the sample concentrations on the *X*-axis. All observations were done in triplicate to obtain the mean values.

2.7.2. Phosphomolybdate assay. The total antioxidant capacity of the samples was assessed by the phosphomolybdate reduction method,[25] with ascorbic acid used as the reference antioxidant. Briefly, 0.3 mL of each sample was mixed with 3.0 mL of phosphomolybdate reagent composed of 0.6 M sulfuric acid, 28 mM sodium phosphate, and 4 mM ammonium molybdate. The reaction mixtures were incubated at 95 °C for 90 min and subsequently cooled to room temperature. Absorbance was measured at 695 nm against a reagent blank. Antioxidant capacity was determined using the ascorbic acid calibration curve ($y = 3.0909x$, $R^2 = 0.9744$) and expressed as mg ascorbic acid equivalents (AAE).

2.7.3. Ferric reducing power assay. The reducing potential of the samples was determined using the ferric ion reduction assay based on the potassium ferricyanide–trichloroacetic acid system, with ascorbic acid serving as the standard.[26] In brief, 1.0 mL of sample solution was combined with 2.5 mL of phosphate buffer (0.2 M, pH 6.6) and 2.5 mL of potassium ferricyanide (1%, w/v). The mixture was incubated at 50 °C for 20 min, after which the reaction was terminated by adding 2.5 mL of trichloroacetic acid (10%, w/v). Following centrifugation, the supernatant was diluted with distilled water and treated with ferric chloride solution (0.1%, w/v). The absorbance was measured at 700 nm, and reducing power was calculated from the ascorbic acid standard curve ($y = 5.492x + 0.566$, $R^2 = 0.9729$), with results expressed as mg ascorbic acid equivalents (AAE).

2.8. Metal ion release study

The quantification of copper ions (Cu^{2+}) and selenium ions (Se^{4+}) released from CuO/SeO_2 NCs and CuO/SeO_2/polysaccharide NCs was carried out to evaluate their possible contribution to antibacterial activity. Briefly, 10 mg of each nanocomposite was suspended in 10 mL of Mueller–Hinton (MH) broth and incubated at 37 °C. The suspension was then shaken gently at 100 rpm in an incubator at 37 °C. After a certain period of time (0, 1, 3, 6, 12, 24, and 48 hours), 1 mL of each solution was taken out by a syringe and then centrifuged at 12 000 rpm for 10 minutes. The supernatant was then filtered through a 0.22-μm syringe filter to obtain only the dissolved ions in solution form. The amount of each of the above ions was detected by inductively coupled plasma mass spectroscopy (ICP-MS; Agilent 7700 Series ICP-MS System; Agilent Technologies, Santa Clara, CA, USA), with standard copper and selenium solution as the reference solution. All measurements were carried out in triplicate. The results were plotted as mean values ± standard deviation. The quantified amount of each of these

ions was plotted as a function of time to compare the ion release characteristics of uncoated and polysaccharide-functionalized NCs.

2.9. Agar well diffusion method

The agar well diffusion method[27] was used for the determination of the antibacterial activity of clove extract and nanocomposites. Briefly, 100 μL of bacterial suspension (*ca.* 1×10^8 CFU mL^{-1}) was uniformly inoculated onto the surface of Mueller–Hinton agar plates with a sterile spreader. Wells of 9 mm diameter were aseptically punched into the agar, and 100 μL of each test sample at the desired concentration was introduced into the wells. Ciprofloxacin (5 μg) and sterile distilled water served as a positive and a negative control, respectively. Plates were incubated at 37 °C for 18–24 h or as required for the development of the particular strain under test. Antibacterial activity was assessed from the diameter of the inhibition zones surrounding the wells in millimeters. All the experiments were performed in triplicate and reported as mean ± SD.

2.10. Cytotoxicity

2.10.1. Cell lines and culture conditions. Human cancer cell lines, including PC3 (human prostate adenocarcinoma), HeLa (human cervical adenocarcinoma), HT-29 (human colorectal adenocarcinoma), and A549 (human lung adenocarcinoma epithelial cell line), as well as the normal WI-38 cell line (human lung fibroblasts), were employed in the present study. All cell lines were obtained from the Cell Culture Unit at the Egyptian Liver Research Institute and Hospital (ELRIAH Institute, Sherbin, Dakahlia Governorate, Egypt), where they were routinely maintained and propagated under standard cell culture conditions in accordance with the supplier's recommended protocols for experimental research applications. The cells were maintained at 37 °C in a humidified 5% CO_2 incubator. All cell lines were grown in DMEM (Cat# 11965-092, Thermo Fisher Scientific, Waltham, MA, USA) supplemented with 10% FBS (Cat# 16000-044), 100 U per mL penicillin, and 100 μg per mL streptomycin (Cat# 15140-122). Subculturing was made at 80–90% confluence, and only the cultures with passage numbers lower than 15 were used for the cytotoxicity experiments.

The cells were exposed for 48 h to either Cu/SeO_2 NC or Cu–SeO_2/polysaccharide NC. For phase-contrast imaging, this was done at 24 and 48 h. Concentration ranges were selected based on IC50 and IC50/2 values reported in Hassan *et al.*[28] and Elattar *et al.*[29]

2.10.2. MTT cell viability assay. The cytotoxic effects of the nanocomposites were quantified using the MTT assay (Cat# M6494, Thermo Fisher Scientific, USA). PC3, HeLa, HT-29, A549, and WI-38 cells were seeded in 96-well plates (Cat# 3599, Corning, NY, USA) at a density of 5×10^3 cells per well and allowed to adhere overnight.

The cells were incubated for 48 h with a gradient concentration of Cu/SeO_2 NC, CuO/–SeO_2/polysaccharide NC, and purified propolis polysaccharides. Afterwards, 20 μL of MTT at 5 mg mL^{-1} was added to each well, and the plates were placed in an incubator for 4 h to allow formazan to form. After incubation, the medium was discarded and crystals dissolved in 150 μL DMSO (Cat# D8418, Sigma-Aldrich, St. Louis, MO, USA). The resulting absorbance was measured at 570 nm using a SpectraMax M5 microplate reader (Molecular Devices, San Jose, CA, USA). Cell viability was calculated relative to untreated controls. IC_{50} values were derived using nonlinear regression in GraphPad Prism following standard protocols.[30]

The Selectivity Index (SI) was calculated to evaluate the preferential cytotoxicity of the synthesized nanocomposites toward cancer cells relative to normal cells. SI was calculated using equation (eqn (2)):

$$SI = \frac{IC_{50}(\text{normal cells})}{IC_{50}(\text{cancer cells})} \quad (2)$$

where IC_{50} values were obtained from *in vitro* cytotoxicity assays using WI-38 normal fibroblasts and the corresponding cancer cell lines. Higher SI values indicate greater selectivity toward cancer cells.

2.11. Statistical analysis

All experiments were performed in triplicate ($n = 3$), and results are presented as mean ± standard deviation (SD). IC_{50} values were determined using nonlinear regression analysis. Statistical analysis was performed using one-way ANOVA followed by Tukey's *post hoc* test, with significance set at $p < 0.05$. For antibacterial assays, statistical comparisons were conducted independently for each bacterial strain to evaluate differences in inhibition zone diameters among the tested samples.

3 Results and discussion

3.1. Proposed mechanism of nanocomposites formation

3.1.1. Formation of CuO/SeO_2 nanocomposite (CuO/SeO_2 NC). The green synthesis of the CuO/SeO_2 nanocomposite proceeds *via* a biomolecule-mediated redox, complexation, and nucleation mechanism driven by the phytochemical constituents from clove extract, which is rich in polyphenols, such as eugenol, flavonoids, and organic acids (Fig. 1). It begins with the dissociation of aqueous copper sulfate, releasing Cu^{2+} ions, while selenium dioxide is hydrated to form selenous acid species, H_2SeO_3/SeO_3^{2-}. The phenolic hydroxyl and methoxy groups in clove extract serve as chelating and mild reducing agents, coordinating with Cu^{2+} ions through oxygen donor sites, promoting controlled hydrolysis. On heating and adjusting the pH, such Cu-phytochemical complexes undergo dehydration and oxidation, developing nucleation of CuO nanoparticles with stabilization by residual plant-derived ligands.[25] Simultaneously, SeO_2 species interact with growing CuO nuclei through shared oxygen atoms, thus promoting the development of Cu–O–Se interfacial bonds.[26] These phytochemicals control the growth kinetics, limit particle agglomeration, and favor intimate contact between CuO and SeO_2 domains instead of phase segregation. This leads to the formation of a heterostructured CuO/SeO_2 nanocomposite that predominantly possesses Cu^{2+}

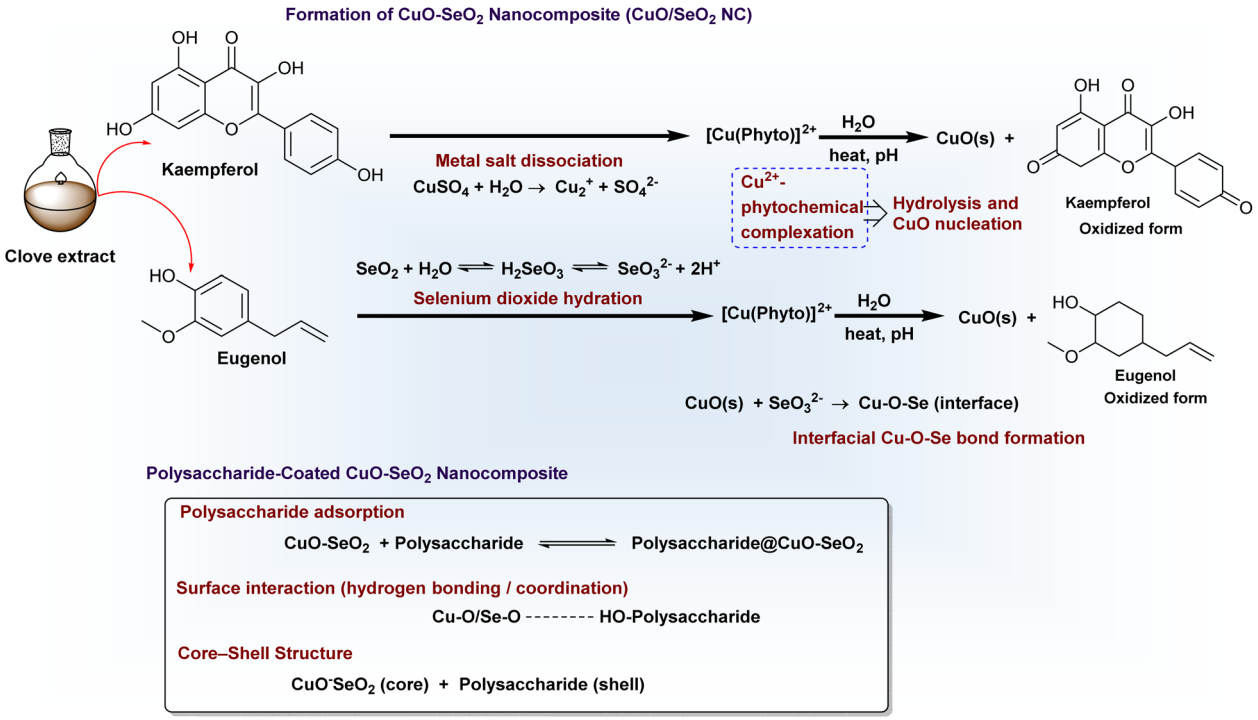

Fig. 1 A schematic representation of the proposed green synthesis mechanism for the CuO–/SeO_2 nanocomposite and its polysaccharide coating architecture is presented. The Cu^{2+} ion complexation, through phytochemicals, and its controlled hydrolysis in the presence of hydrated SeO_2 species, provide a pathway to CuO nucleation and subsequent interfacial Cu–O–Se bond formation, giving rise to a heterostructured CuO–/SeO_2 nanocomposite. Further, the adsorption of polysaccharides with ample hydroxyl and carboxyl groups produces a stable core–shell-like CuO/SeO_2/polysaccharide NC without changing the oxidation states of Cu^{2+} and Se^{4+}.

and Se^{4+} as the main oxidation states, which agrees with the obtained results of XPS.

3.1.2. Synthesis of CuO/SeO_2/polysaccharide NC. In the second step, polysaccharides were introduced simultaneously with the clove extract before the addition of the metal precursors, indicating that surface functionalization occurs concurrently with nanocomposite formation rather than a post-formation process. Under these conditions, the polysaccharide chains may be involved in the nucleation and growth of the nanocomposites by interacting with Cu^{2+} and SeO_2-derived species *via* their hydroxyl, ether, and carboxyl groups. These interactions enable coordination with the surface Cu–O and Se–O functionalities, as well as steric stabilization.[20,21] This helps control particle growth, prevent aggregation, and enable the formation of a more ordered nanostructure (Fig. 1). Furthermore, the matrix of the polysaccharide may act as a soft template directing nanostructure formation. This would enable control of the spatial distribution of the inorganic components without affecting their inherent chemical composition. Crucially, the analysis using X-ray photoelectron spectroscopy (XPS) indicated that the oxidation states of copper and selenium were maintained at Cu^{2+} and Se^{4+}, respectively. This is evident from the persistence of the Cu 2p satellite peaks and the characteristic Se 3d peaks. This indicates that although the polysaccharide is involved in the synthesis of the CuO/SeO_2 nanostructure, it does not affect the redox pathway of the formation of CuO/SeO_2; it is likely functioning as a stabilizer. The resulting product can be described as a hybrid organic–inorganic nanocomposite, where the CuO/SeO_2 core is synthesized *in situ* in the presence of the polysaccharide, followed by the formation of a polysaccharide-rich shell by virtue of strong interfacial interactions and hydrogen bonding. This provides indirect evidence of a core–shell-like structure with improved structural stability and dispersion properties.

3.2. Characterization of nanocomposites

3.2.1. XPS analysis. The XPS profiles of the CuO/SeO_2 NC demonstrated the successful coexistence of copper, oxygen, selenium, and residual carbon species, verifying the formation of a mixed-metal oxide system (Fig. 2a–e). The Cu 2p spectrum displayed a main Cu $2p_{3/2}$ peak at *ca.* 934–935 eV with characteristic satellite bands between 940–945 eV, consistent with Cu^{2+} in CuO, reported by Poulston *et al.*[31] and Würz *et al.*,[32] confirming that copper predominantly exists in the Cu^{2+} (CuO) oxidation state and that no Cu^0 or Cu^+ signatures are detectable, indicating strong thermodynamic stabilization of Cu^{2+} within the oxide lattice. In the O 1s region, there are two components: 532.0 and 533.2 eV for lattice oxygen (Cu–O/Se–O) and surface hydroxyls, respectively, similar to typical oxide–hydroxide distributions in mixed oxide systems. Selenium exhibits multiple 3d components between 55–61 eV, matching Se^{4+} (SeO_2-like species) and minor reduced states, as expected based on reported Se 3d binding energies for SeO_2-based systems from Reddy *et al.*[33] The high contribution of lattice oxygen (58.1%)

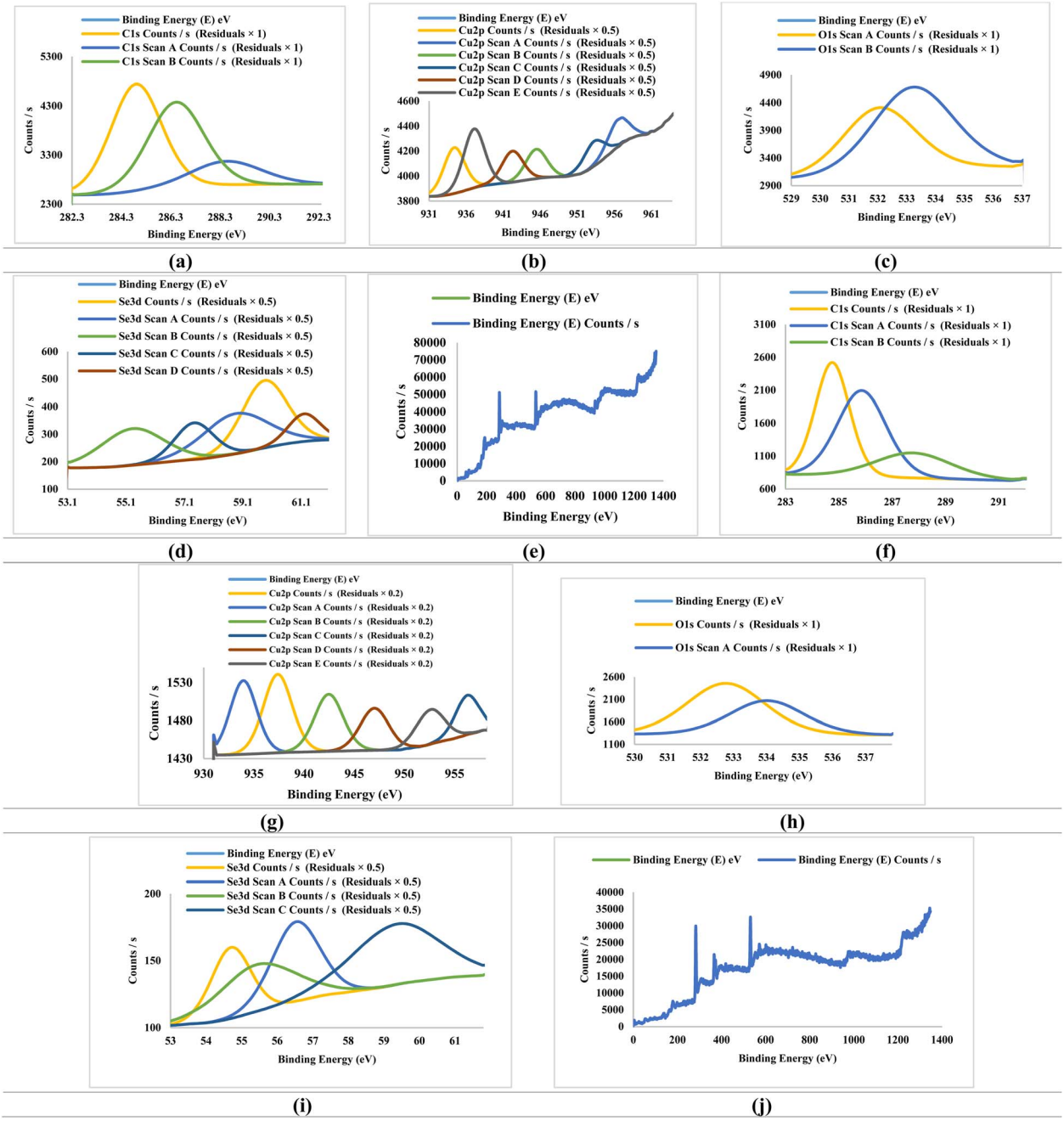

Fig. 2 XPS spectra of (a–e) CuO/SeO_2 NC and (f–j) polysaccharide-functionalized CuO/SeO_2 NC showing high-resolution scans for C 1s (a and f), Cu 2p (b and g), O 1s (c and h), Se 3d (d and i), and overall survey scans (e and j), confirming successful core formation and surface modification.

together with the dominant Se^{4+} signal confirms the integrity of the metal-oxide framework and suggests a well-developed CuO/SeO_2 interfacial interaction rather than phase-segregated domains.

Significant spectral changes were observed upon polysaccharide coating (Fig. 2f–j). As such, the C 1s envelope developed increased intensities at 284.7, 285.8, and 287.8 eV corresponding to C–C/C–H, C–O, and O–C=O groups, respectively, demonstrating successful incorporation of oxygenated carbohydrate functionalities, similar to the spectral features described by Kesavan *et al.*[34] for polysaccharide-functionalized nanomaterials. Concomitantly, the O 1s peak shifted to higher binding energies ranging from 532.8–534.0 eV, reflecting increased contributions from C–O–C and C–OH moieties of the polysaccharide matrix. It further indicates the formation of new interfacial hydrogen-bonding networks between surface oxides and polysaccharide hydroxyl groups, which could contribute to stability in nanocomposites under aqueous conditions. The Cu 2p region retained its Cu^{2+} satellite structure, indicating that surface functionalization did not reduce or otherwise alter the CuO core, an important indicator of structural robustness under green synthesis conditions.

In turn, the general shift of the Se 3d signals toward lower BE (*ca.* 54–59 eV) and the redistribution of the Se oxidation states support partial complexation or stabilization of the Se species by polysaccharide hydroxyls. Additional confirmation of their expected elemental composition comes from survey spectra for both samples, where polysaccharide wrapping increases the carbon atomic % from 68.7% to 72.6% and decreases the relative metal signal intensities due to surface shielding. That is, this attenuation effect strongly supports the formation of a continuous organic coating. Thus, these findings confirm that the polysaccharide behaves as a stable passivating layer that does not disrupt the integrity of the CuO/SeO_2 core structure. These findings are in good agreement with the literature observations in analogous green-synthesized or biopolymer-wrapped hybrid nanomaterials. Besides, the preserved oxidation states and similar peak shapes indicate strong compatibility between the inorganic core and the biopolymer layer, which is of use toward biomedical, catalytic, and environmental applications requiring colloidal stability and minimized leaching of metal ions.

3.2.2. UV-Vis spectroscopy. The optical behavior of the synthesized materials was characterized by UV-Vis spectroscopy, and the spectra are shown in Fig. 3a and b. The extract of clove exhibited a characteristic peak at 426 nm with a moderate absorbance of 0.530, which can be attributed to the occurrence of flavonoids and polyphenolic compounds as inherent reducing and stabilizing agents. With the addition of CuO and SeO_2 to form the CuO/SeO_2 NC, a red-shifted absorption band at 428 nm was observed with higher absorbance at 0.589, reflecting greater electronic interaction between CuO and SeO_2 phases. The red shift suggests enhanced interfacial charge transfer and possible band structure modification arising from CuO/SeO_2 heterojunction formation and polysaccharide-induced surface states, which contribute to improved visible-light absorption and photocatalytic performance.[35]

Notably, CuO/SeO_2/polysaccharide NC showed a stronger red shift at 474 nm with an absorbance of 0.959. This is attributed

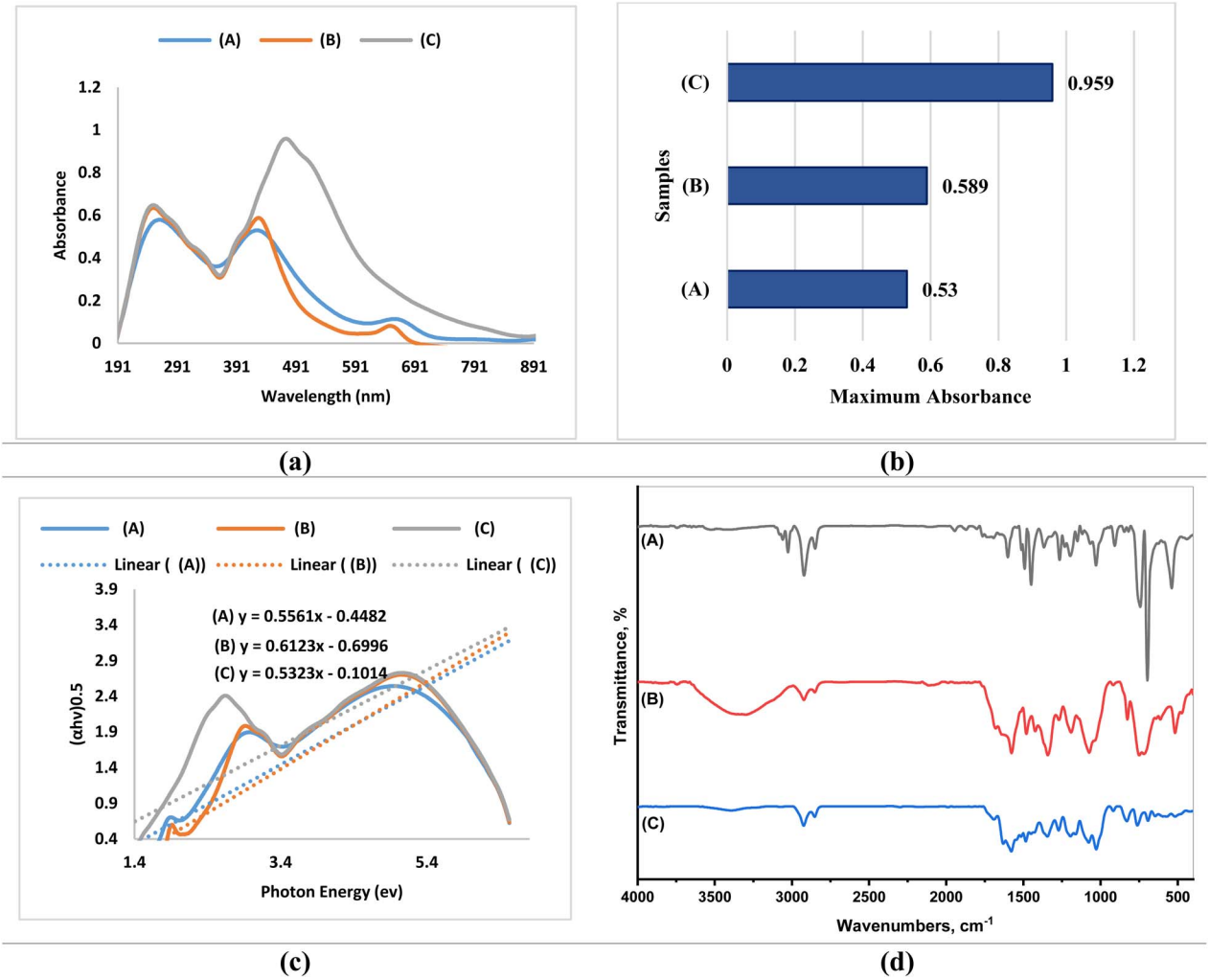

Fig. 3 (a) UV-Vis spectroscopy of plant extract and nanocomposites. (b) Maximum absorbance recorded by each sample. (c) Tauc plotted photon energy (eV) *versus* $(\alpha h\nu)^{0.5}$. (d) FTIR spectral analyses of plant extract and nanocomposites. (A) Clove extract; (B) CuO/SeO_2 NC; (C) CuO/SeO_2/polysaccharide NC.

to the effective capping and stabilizing effect of the polysaccharide matrix, which prevented the agglomeration of the nanoparticles as well as enabled better dispersion of active sites. Such polysaccharide-induced stabilization of selenium nanostructures has been found to extend light absorption and increase bioactivity.[36] The red shift observed in the case of CuO/SeO_2/polysaccharide NC thus indicates the cooperative action of the polysaccharide to influence the optical behavior of the nanocomposite.

The optical band gap (E_g) was also determined by Tauc's relation. The linear region of Tauc plots produced the following equations: $y = 0.5561x - 0.4482(A)$, $y = 0.6123x - 0.6996(B)$, and $y = 0.5323x - 0.1014(C)$ (Fig. 3c). The trend was such that the addition of SeO_2 into the CuO matrix decreased the band gap, and subsequent addition of the polysaccharide decreased it further, hence enhancing visible-light harvesting. This discovery is aligned with Syrek *et al.*,[35] who reported that CuO/SeO_2-based heterostructures optimize light utilization efficiency in sunlight-driven processes. Similarly, Alamri[37] demonstrated that green-synthesized CuO/SeO_2 nanocomposites have lower band gap values than pure oxides and are therefore suitable for catalytic and antibacterial functions.

These results collectively define that the incorporation of polysaccharides in the CuO/SeO_2 system has a profound effect on its optical properties, producing a stable nanocomposite hybrid with increased visible-light absorbance. The improvement can be attributed to the synergistic interaction among phytochemicals, metal oxides, and the backbone of the polysaccharide, which altogether optimize the electronic structure and interfacial charge transfer kinetics. These aspects serve key roles in photocatalytic applications, energy harvesting, and biomedical applications.[35–37]

3.2.3. FTIR spectral analyses. FTIR spectroscopy was conducted to identify functional groups in the clove extract and confirmation of the formation and surface modification of the CuO/SeO_2 and CuO/SeO_2/polysaccharide nanocomposites, as shown in Fig. 3d and Table S1. The FTIR spectrum of the clove extract revealed characteristic signals attributed to phenolic and aromatic phytoconstituents, wherein strong bands at 3058 and 3025 cm^{-1} were related to aromatic =C–H stretching vibrations. The absorption bands at 2923 and 2848 cm^{-1} were related to aliphatic C–H stretching, while the strong band at 1601 cm^{-1} was attributed to aromatic C=C stretching typical of eugenol-rich clove extracts. Other features observed at 1514, 1489, 1448, and 1367 cm^{-1} corresponded to C–O and C–H bending of phenylpropanoid groups, consistent with previous reports on clove-mediated synthesis of nanoparticles.[27] Absorption bands in the fingerprint region (1264–537 cm^{-1}) correspond to the abundance of oxygenated functional groups capable of reducing and stabilizing the metal ion for nanoparticle formation.

The FTIR spectrum of CuO/SeO_2 NC revealed remarkable changes as compared to that of the plant extract, confirming the formation of a hybrid metal/oxide nanostructure. The broad and intensive bands ranged around 3360–3299 cm^{-1} and corresponded to O–H stretching, which may come from absorbed water or from residual phytochemicals on the surface of nanoparticles. The absorption bands at 2921 and 2851 cm^{-1} corresponded to aliphatic C–H stretching, whereas strong absorptions at 1689 and 1644 cm^{-1} corresponded to C=O and C=N stretching, reflecting plant-derived ligands coordinating with the surface of CuO/SeO_2. Interestingly, the presence of bands at 1577, 1482, 1426, and 1369 cm^{-1} confirmed aromatic C=C and C–O vibrations. More importantly, the emergence of bands in the low-frequency region at 613, 518, 469, and 391 cm^{-1} is characteristic of metal–oxygen and Se–O stretching, providing strong evidence for the formation of CuO and SeO_2. These features are in accordance with FTIR patterns reported in the literature for biosynthesized SeO_2-based nanomaterials and Cu–Se hybrid composites.[37,38]

The shifting and intensity changes of additional bands in the spectrum of CuO/SeO_2/polysaccharide NC confirmed that polysaccharides had been grafted on the surface of nanoparticles. The broadening and shifting of the O–H stretching band to 3387 cm^{-1} revealed an improvement in hydrogen bonding between the biopolymer and oxide nanoparticles. The absorption bands related to aliphatic C–H were still observed at 2924 and 2851 cm^{-1}, while overlapped carbonyl- and amide-related bands at 1689–1635 cm^{-1} demonstrated strong interactions between CuO/SeO_2 and the polysaccharide functional groups. Diagnostic bands of polysaccharides at 1270, 1221, 1194, 1155, 1074, and 1028 cm^{-1} proved the presence of C–O–C and C–O stretching vibrations, typical of polymeric carbohydrates. As compared to the binary CuO/SeO_2 nanocomposite, several metal–oxygen and Se–O bands (for example, 648, 569, and 518 cm^{-1}) showed decreased intensities or were slightly shifted, demonstrating the partial shielding effect of the polysaccharide coating on the surface. The spectral shifts, new functional-group signatures, and changes in band intensities observed across the three samples together provide strong evidence for successful reduction and stabilization of CuO/SeO_2 NC by the clove extract, followed by surface functionalization with the polysaccharide matrix. These results agree well with previous FTIR-based analyses of similarly prepared plant-mediated and polysaccharide-modified metal–selenium nanostructures,[27,37,38] confirming the structural integrity and effective capping behavior of the biogenic components used in this study.

3.2.4. Zeta potential and DLS analysis. Colloidal stability and surface functionalization were evaluated by zeta potential measurements for the synthesized nanocomposites, which are represented in Fig. 4. Zeta potential measurements were carried out under controlled conditions of ionic strength and near-neutral pH (aqueous medium), with recorded conductivity and viscosity values to ensure reliable comparison between samples. These controlled conditions allow for consistent evaluation of surface charge and colloidal stability of the nanocomposites. For CuO/SeO_2 NC, the measured zeta potential was −15.1 mV with a viscosity of the dispersion medium of 0.900 mPa s and conductivity of 0.876 mS cm^{-1}, while the electrophoretic mobility was −0.000116 $cm^2\ V^{-1}\ s^{-1}$ (Fig. 4a). This relatively low negative charge indicates limited electrostatic repulsion and is an indication that the uncapped nanocomposite has a relatively weakly stabilized colloidal structure

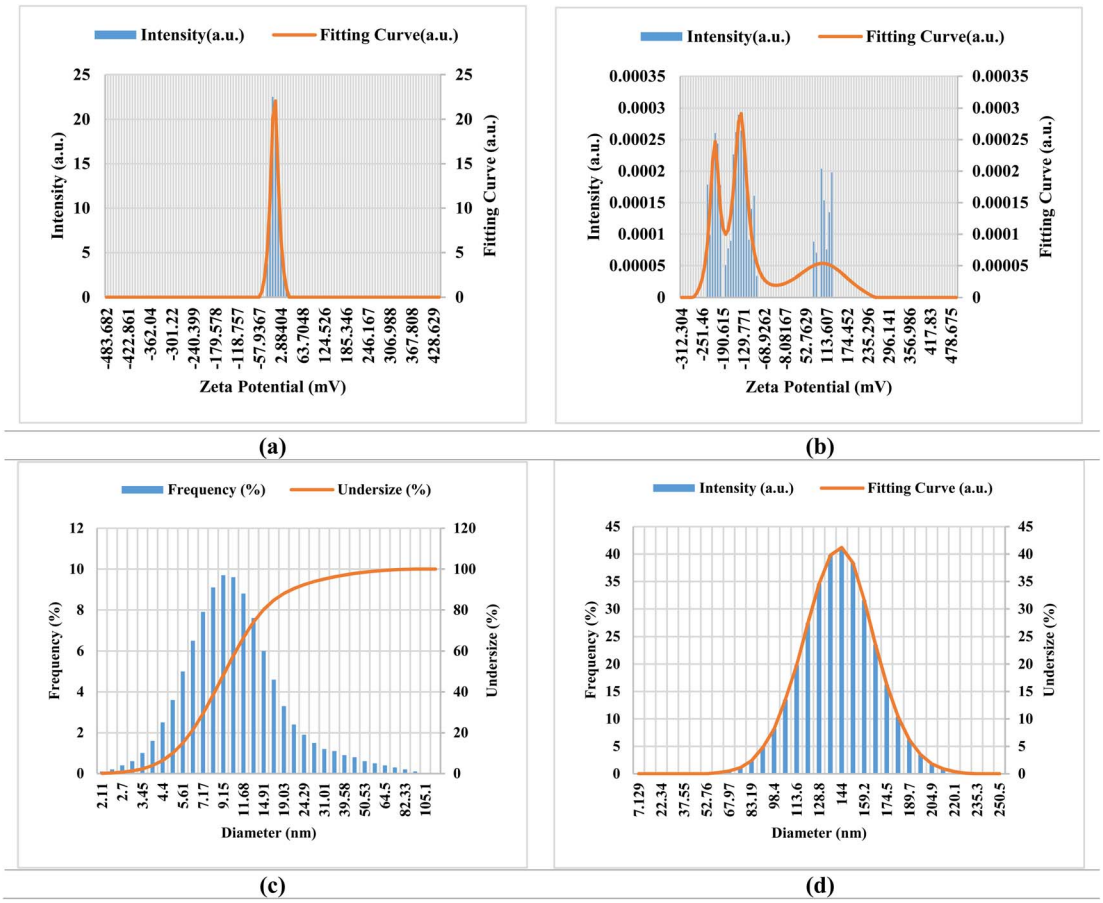

Fig. 4 Zeta potential and particle size distribution analyses of (a and c) CuO/SeO_2 NC and (b and d) CuO/SeO_2/polysaccharide NC. The uncapped CuO/SeO_2 NC displayed a zeta potential of −15.1 mV, with an electrophoretic mobility of −0.000116 $cm^2\ V^{-1}\ s^{-1}$ and conductivity of 0.876 mS cm^{-1}, reflecting its weak colloidal stability because of limited surface charge density. On the contrary, the polysaccharide-functionalized CuO/SeO_2 NC revealed a highly negative zeta potential of −139.8 mV, coupled with an increased electrophoretic mobility (−0.001082 $cm^2\ V^{-1}\ s^{-1}$) and conductivity (1.286 mS cm^{-1}), proving the effective capping of polysaccharides on the NC and eventual enhancement of its colloidal stability.

and thus has a greater tendency to aggregate. Similar observations have been reported for metal oxide–selenium systems lacking strong polymeric stabilizers, where the surface charge alone was insufficient to maintain long-term suspension stability.[39]

By contrast, the CuO/SeO_2/polysaccharide nanocomposite exhibited a remarkably high zeta potential of −139.8 mV with a viscosity of 0.895 mPa s, conductivity of 1.286 mS cm^{-1}, and an electrophoretic mobility of −0.001082 $cm^2\ V^{-1}\ s^{-1}$ (Fig. 4b). The strong increase in the negative surface charge after polysaccharide addition evidences that effective capping occurs with strong surface functionalization. Such a high negative zeta potential may arise from the high density of ionizable hydroxyl and carboxyl groups in the polysaccharide matrix; however, further validation under varying ionic strengths is recommended. This enhanced negative charge, through electrostatic repulsion, resulted in outstanding colloidal stability with the prevention of coalescence of particles and uniform dispersion. Similar stabilization has been reported for selenium or metal-based nanomaterials capped with biopolymers such as chitosan, gum Arabic, and fungal- or plant-based polysaccharides, which greatly increase the magnitude of zeta potential and improve the stability of the dispersions.

Further support for the presence of abundant surface-bound ionic groups and enhanced charge mobility arises from the markedly higher conductivity observed for the polysaccharide-capped system. This behavior is in good agreement with reports showing that polysaccharide-stabilized selenium nanostructures exhibit improved electrophoretic mobility due to the strong interaction between biopolymer functional groups and nanoparticle surfaces.[36] Moreover, polysaccharide-mediated synthesis usually produces nanoparticles with increased biocompatibility, antioxidant capacity, and biological activity, which in turn are linked with strongly negative zeta potential values.[40] Briefly, the clear outcome from the measurement of zeta potential upon polysaccharide capping is that the original weakly stable CuO/SeO_2 system was transformed into a highly stable nanocolloidal suspension. This agrees with previous works dealing with the importance of biopolymer stabilizers to

enhance nanoparticle stability, surface charge density, and functional performance.[36,39,40]

The particle size distribution and colloidal nature of the synthesized nanocomposites were also assessed using dynamic light scattering (DLS) measurements. For the CuO/SeO_2 nanocomposite, the average hydrodynamic diameter was found to be 13.44 nm, slightly higher than the observed size from the HR-TEM measurements (9.0–25.0 nm) (PDI = 0.385) (Fig. 4c). This difference arises because DLS measures the hydrodynamic diameter, including the solvation layer and loosely associated phytochemicals on the surface. For the CuO/SeO_2/polysaccharide nanocomposite (Fig. 4d), the distribution and size of the hydrodynamic diameter are narrower and smaller, at 10.2–12.8 nm (PDI = 0.192), as opposed to the HR-TEM measurements, where the size ranged from 4.5 to 8.2 nm.

The reduction in size and distribution with the incorporation of the polysaccharide also indicates the effective control of nucleation and growth, leading to well-dispersed nanoparticles. Moreover, the significant increase in the absolute value of the zeta potential from −15.1 mV to −140.2 mV clearly indicates the improvement in the stability of the colloids with the incorporation of polysaccharide, mainly due to the presence of ionizable groups of polysaccharide, which provide strong electrostatic repulsion between particles. Therefore, based on the HR-TEM and zeta potential studies, DLS results indicate that polysaccharide-functionalized nanocomposites are not only smaller and more uniform but also highly stable with good dispersion in aqueous media.

The high absolute value of zeta potential and narrow size distribution of DLS indicate good colloidal stability of the polysaccharide-functionalized nanocomposite, although a detailed long-term stability evaluation is still required, which will be considered in future studies.

3.2.5. HR-TEM. HR-TEM micrographs of CuO/SeO_2 NC: Fig. 5a–c shows densely packed, electron-dense nanoparticles forming large and irregular aggregates. Primary particles show heterogeneous morphologies, which range from polyhedral structures up to semi-spherical forms with dimensions extending up to several tens of nanometers. Extensive clustering is an indication of strong interparticle interaction along with high surface energy, leading to the formation of fused domains. The high crystallinity of the composite is confirmed by the distinct lattice boundaries and well-defined crystalline facets observed at higher magnifications, as shown in Fig. 5b and c. This intimate structural contact between the CuO and SeO_2 phases strongly suggests the development of heterogeneous interfacial regions.[41] Similar observations have been associated with enhanced electrochemical and catalytic performance, since interfaces provide rapid charge transfer pathways and improve redox activity in bimetallic or metal oxide–selenide systems. Such interfacial synergy is a keystone for functional applications, including lithium/sodium storage and catalytic transformations, where electron mobility and surface reactivity play key roles. This demonstrates the general aggregation trend in CuO/SeO_2 NCs, which agrees with previous research showing dense clustering of the same green-synthesized metal–selenium oxide system, especially if no capping or stabilizing agent has been used during the synthesis process.[37] Although aggregation reduces surface accessibility, it also enhances structural integrity and upholds crystalline connectivity, potentially advantageous in electronic applications.

In contrast to the binary material, the morphology of the CuO/SeO_2/polysaccharide NC, Fig. 5d–f, is vastly different, evidencing the strong structural effect of the natural polysaccharide additive. HR-TEM images reveal substantially smaller and more regular spherical nanoparticles distributed within a loosely associated, porous, and branched network. The resulting architecture is sharply different from the densely fused masses in the CuO/SeO_2 NC, indicating that the polysaccharide effectively restricts uncontrolled particle growth. The polymeric matrix here acts as a bio-template and stabilizer, spatially separating nanoparticles and preventing their hard agglomeration.[42] This behavior is consistent with the fact that polysaccharides, due to their abundant functional groups, are effective in the chelation, nucleation, and steric stabilization of metal or metal oxide nanoparticles, leading to hybrid materials with better dispersions and structural homogeneities. This is in good agreement with the enhanced distribution of nanoparticles in the polysaccharide hybrid.

It is also visible that at higher magnification (Fig. 5f), CuO/SeO_2 nanoparticles can be clearly observed with electron-dense cores and a lighter contrast shell. This suggests the presence of a core–shell-like structure. However, it is difficult to clearly distinguish the polysaccharide shell because of its low electron density. To further confirm this structure, we also conducted line-scan EDX mapping on individual nanoparticles. A specific distribution pattern is visible in which Cu and Se are concentrated at the core of nanoparticles. On the other hand, carbon signals corresponding to polysaccharides are concentrated at the outer part of nanoparticles. This provides supporting evidence for a core–shell-like structure.

The prepared composite presents a highly porous and high-surface-area architecture, while the CuO/SeO_2 nanoparticles remain accessible and well exposed. This kind of morphology is of particular importance in the case of surface-dependent applications, such as sensing, catalysis, and antimicrobial performance, since the polymeric network enhances mass transport and increases the availability of reactive sites. Moreover, the flexible organic scaffold enhances mechanical stability and prevents sintering or particle collapse, which is important for long-term operational durability. Generally, from the HR-TEM results, it is very clear that binary CuO/SeO_2 NC possesses densely aggregated crystalline domains that may favor electronic coupling yet limit accessible surface area. In contrast, the polysaccharide-modified nanocomposite shows better nanoparticle dispersion in spherical geometry and a porous hybrid architecture due to the templating effect of the natural polymer. These observations are in good agreement with literature reports on the usefulness of the polysaccharide–metal oxide hybrid system toward accessing well-controlled morphology and superior functional performance.

3.2.6. SEM. The surface morphology of the prepared CuO/SeO_2 NC was investigated by SEM with a magnification of ×10 000 (Fig. 6a and b). The micrographs indicate that the material

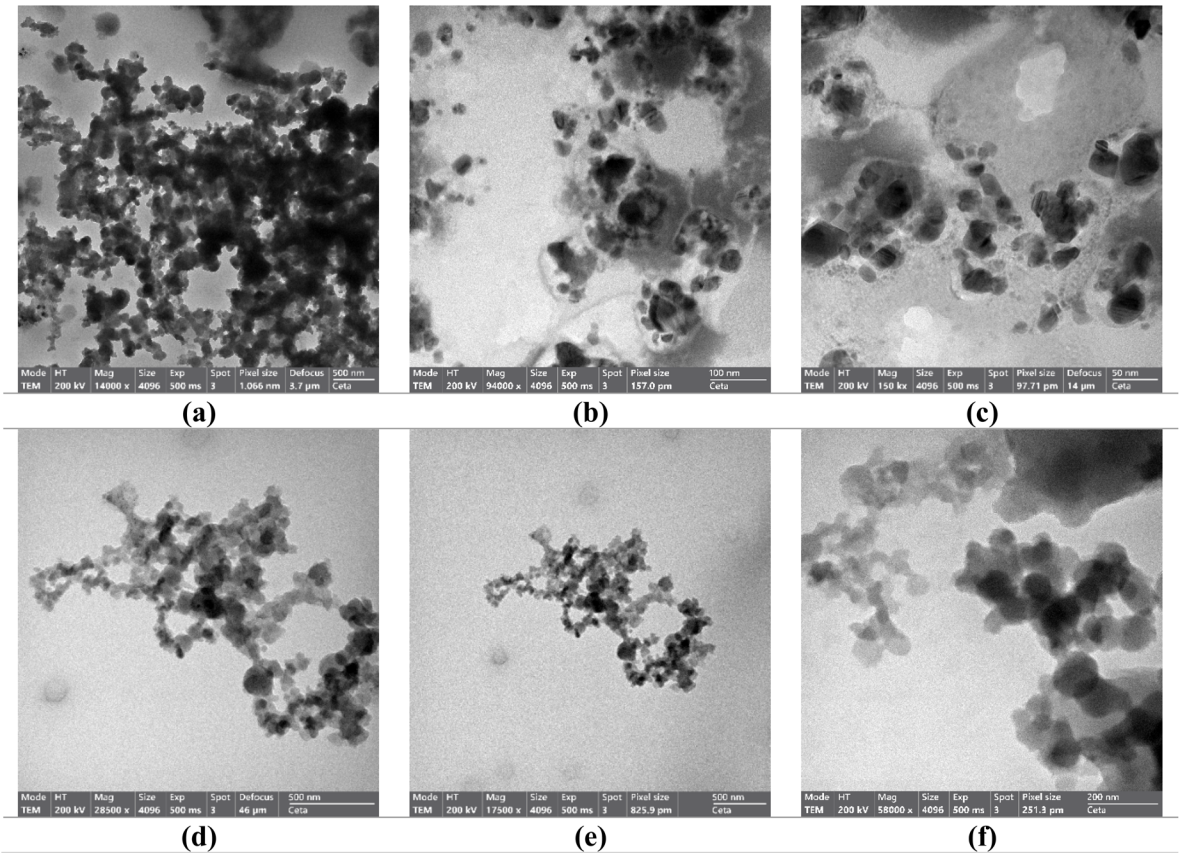

Fig. 5 HR-TEM micrographs of nanocomposites. (a–c) CuO/SeO_2 NC; and (d–f) CuO/SeO_2/polysaccharide NC at 50–500 nm of scale bar.

consists of fine spherical to semi-spherical nanoparticles with a heterogeneous surface. One striking characteristic is that these primary nanoparticles are highly aggregated and agglomerated into large, dense clusters. This behavior is typical of metal oxide–selenium nanomaterials due to their inherently very high surface energy and strong interparticle attractive forces, as already mentioned during the discussion on some mixed CuO/SeO_2 systems for photoactive coating and electrode materials.[35,37]

The surface is appreciated to be quite rough and porous, reflecting the presence of many nano-scale cavities and interparticle voids. This morphology enhances the effective surface area considerably, which is quite favorable towards catalytic and photoelectrochemical applications. Such porous architecture has been demonstrated in various ways to improve light absorption, enhance reaction site availability, and facilitate charge separation, thereby enhancing the performance of CuO/SeO_2-based photoelectrodes.[35] The SEM results, therefore, confirm that the structural characteristics of the binary NC are in concert with those usually called for in high-performance photocatalytic and sensing materials.

SEM micrographs of the CuO/SeO_2/polysaccharide NC, as presented in Fig. 7a and b, further confirm proper integration of the inorganic nanoparticles with the natural polymeric matrix. Similar to the binary system, the ternary NC is also comprised of spherical nanoparticles at ×10 000 magnification; however, introduction of the polysaccharide results in a noticeable structural modification.

The polysaccharide, acting as a biotemplate and stabilizing polymer,[43] produces a more cohesive and interlinked network. The clusters of nanoparticles are still present, but the extent of random agglomeration is reduced. Instead, the micrographs tend to suggest a partial embedding or anchoring of the CuO/SeO_2 nanoparticles within the framework of the polysaccharide. This structural arrangement enhances the stability of the nanocomposite and prevents excessive particle–particle fusion. Indeed, such polysaccharide-mediated stabilization has been demonstrated in the literature to ensure better dispersion, structural integrity, and surface accessibility in metal oxide-biopolymer nanomaterials.[43] Such a polymer-supported architecture would significantly enhance the functional performance of the resulting nanocomposite. First, abundant hydroxyl and carboxyl groups could be provided by polysaccharides, enabling strong coordination interactions with metal oxides and selenides and contributing to improved durability while facilitating electron or molecule transfer processes. Similar improvements have been reported for SeO_2/CuO composites incorporated within organic scaffolds for photoelectrochemical and antibacterial applications. In general, SEM analysis has confirmed that the addition of polysaccharide resulted in a more organized, stabilized, and structurally robust nanocomposite than

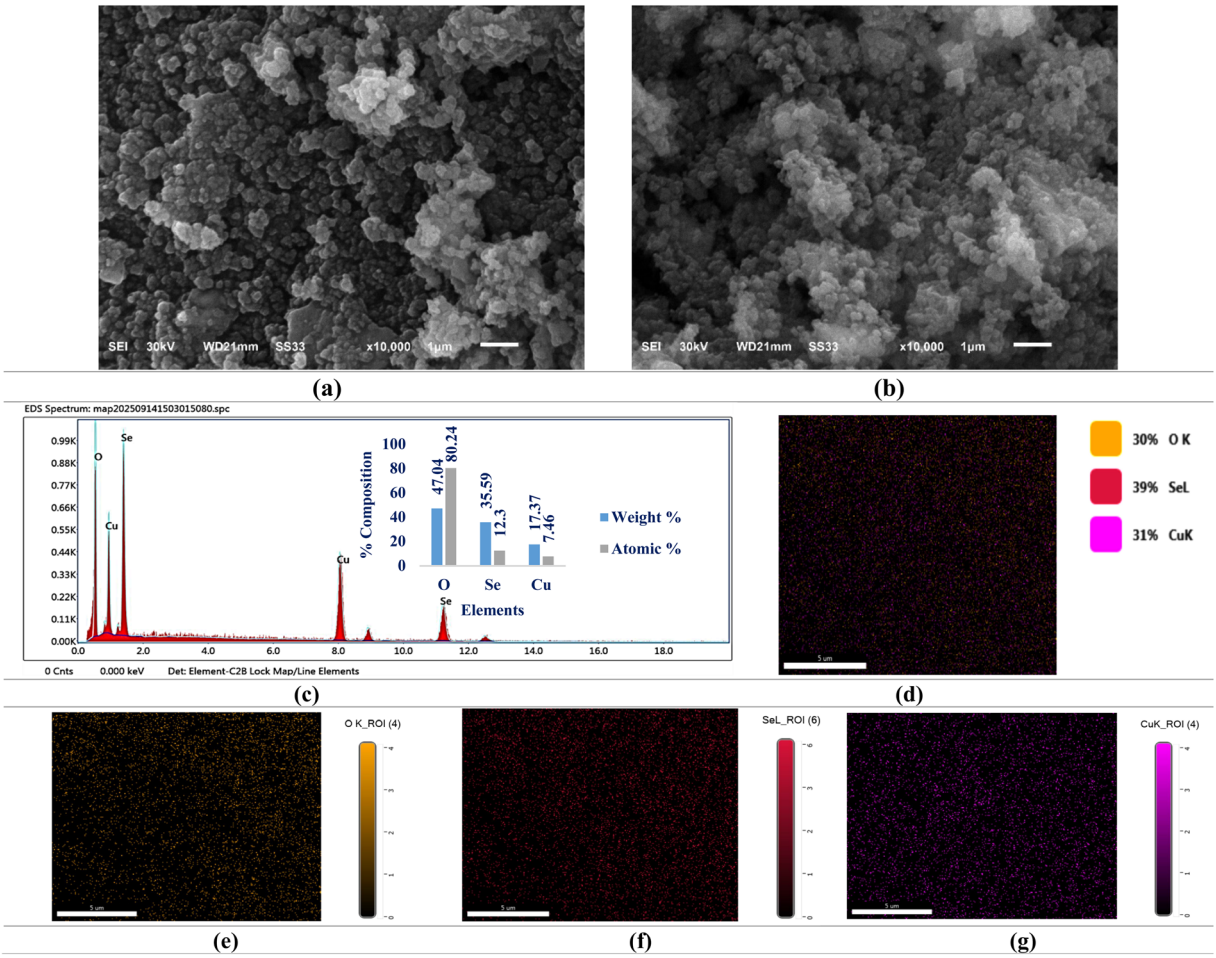

Fig. 6 SEM micrographs, EDX spectrum, and elemental mapping analyses of CuO/SeO_2 NC. (a and b) SEM micrographs of CuO/SeO_2 NC at different magnifications showing spherical nanoparticles and aggregated structures; (c) EDX spectrum confirming the presence of Cu, Se, and O elements; (d) elemental composition analysis showing weight and atomic percentages; (e) oxygen (O), (f) selenium (Se), and (g) copper (Cu) elemental mapping images demonstrating the homogeneous distribution of elements within the nanocomposite.

the binary CuO/SeO_2 system and thus plays a beneficial role in the engineering of nanomaterials with natural biopolymers.

3.2.7. EDX and elemental mapping analyses. Energy-dispersive X-ray spectroscopy has been used to identify the elemental composition and confirm the successful synthesis of the CuO/SeO_2 NC and its polysaccharide-functionalized derivative (Table S2). Fig. 6c and 7c show the EDX spectra of the pristine and functionalized NCs, respectively. It can be observed from both spectra that the expected elements, namely copper (Cu), selenium (Se), and oxygen (O), are present within both nanocomposites, confirming the successful formation of the CuO/SeO_2 framework.

The predominant element in the unmodified CuO/SeO_2 NC was oxygen, which comprised about 47.04 wt% and 80.24 at%, followed by selenium with 35.59 wt% and 12.30 at%, and copper with 17.37 wt% and 7.46 at%, as listed in Table S2. The high atomic percentage of oxygen with respect to its weight fraction is indicative of the construction of an important oxide component, as expected with the CuO/SeO_2 structure. The presence of selenium was identified in quite high amounts, which verifies its successful introduction within the nanocomposite matrix, while the amount of copper represents the contribution of the CuO phase.

The results of functionalization with a polysaccharide showed obvious changes in elemental composition: carbon, which represented the polysaccharide coating, appeared at 28.17 wt% (52.06 at%), therefore confirming the successful surface modification. The oxygen content slightly decreased to 24.20 wt% (33.57 at%), likely due to partial masking of the metal oxide surface by the polysaccharide layer. Cu and Se contents also shifted to 14.37 wt% (5.02 at%) and 33.26 wt% (9.35 at%), respectively, due to the combined effects of surface coating and probable interaction of the polysaccharide with metal oxides. The observed elemental distribution indicates that functionalization does not disturb the core structure of CuO/SeO_2.

As depicted in Fig. 6d–g and 7d–h, the elemental mapping images indicate the homogeneous presence of Cu, Se, and O in pristine as well as in polysaccharide-functionalized CuO/SeO_2 nanocomposites. This further confirms the homogeneous formation of the composite matrix. In the case of the

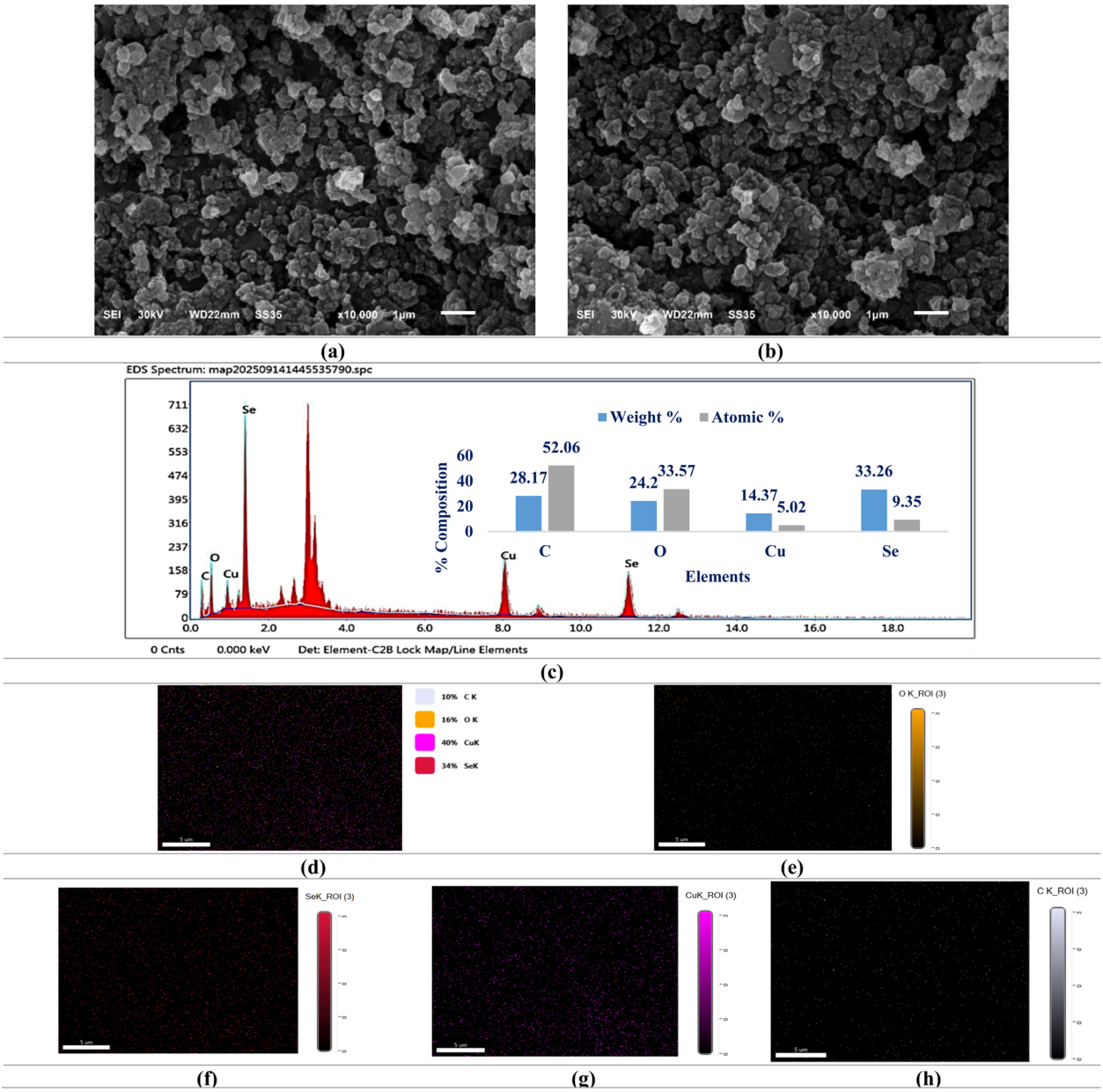

Fig. 7 SEM micrographs, EDX spectrum, and elemental mapping analyses of CuO/SeO_2/polysaccharide NC. (a and b) SEM micrographs of CuO/SeO_2/polysaccharide NC at different magnifications showing polymer-supported nanoparticle networks with enhanced structural cohesion; (c) EDX spectrum confirming the presence of Cu, Se, O, and C elements; (d) elemental composition analysis showing weight and atomic percentages; (e) oxygen (O), (f) selenium (Se), (g) copper (Cu), and (h) carbon (C) elemental mapping images demonstrating the uniform elemental distribution throughout the polysaccharide-supported nanocomposite.

functionalized nanocomposite, carbon was also found to be uniformly distributed and was present along with the metal oxide elements, thereby confirming the successful functionalization of the nanocomposites with the polysaccharide moiety. Furthermore, the presence of a higher amount of carbon also confirms the successful functionalization of the nanocomposites with the polysaccharide moiety, suggesting improved surface coverage and potential stability in aqueous media and the ability of the nanocomposites to interact well with the environment. Furthermore, the presence of copper and selenium at the core region of the nanocomposites, along with a higher amount of carbon at the periphery, suggests a core–shell-like structure of the nanocomposites, as revealed by elemental analysis performed using the EDX technique. However, this observation provides only indirect evidence and cannot conclusively confirm a true core–shell architecture.

3.2.8. XRD analysis. XRD patterns of the CuO/SeO_2 NC and the polysaccharide-functionalized CuO/SeO_2 NC (Fig. 8 and Tables S3, S4) confirmed the formation of well-defined crystalline structures consistent with a rhombohedral phase (space group $R\bar{3}c$, no. 167). The refined lattice parameters for the CuO/SeO_2 NC ($a = b = 4.9588$ Å, $c = 13.5942$ Å) closely match

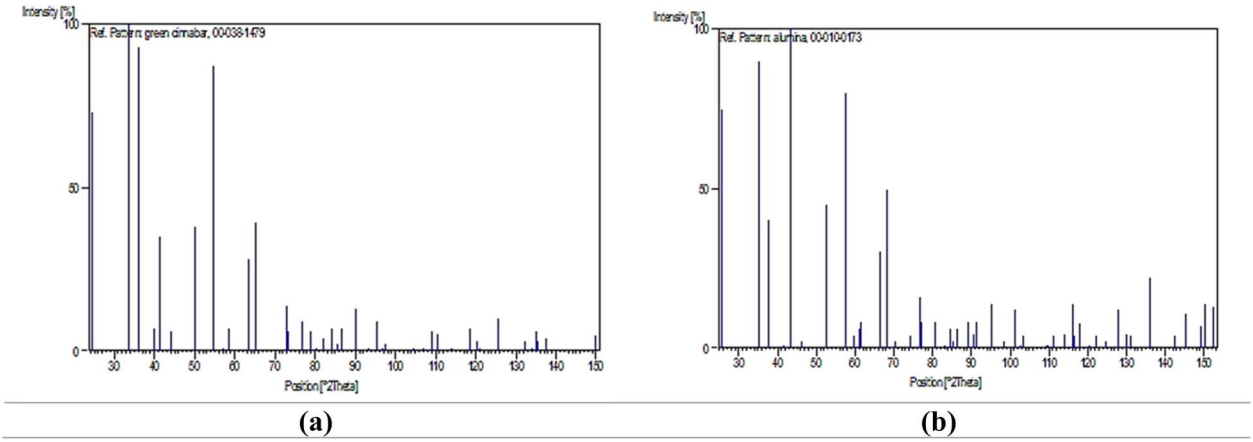

Fig. 8 XRD patterns of (a) CuO/SeO_2 NC and (b) CuO/SeO_2/polysaccharide NC. The CuO/SeO_2 NC exhibits sharp reflections indexed to the SeO_2 phase with space group $R\bar{3}c$, thus confirming its highly crystalline nature and the incorporation of CuO within the host SeO_2 lattice. Indeed, one would expect to observe evident peak shifts, variation in the relative peak intensities, and slight peak broadening in a polysaccharide-functionalized nanocomposite, which account for lattice strain, a reduction in crystallite size, and strong interfacial interactions between the polymeric matrix and the inorganic core. These structural modifications effectively cap the surface while preserving the overall crystalline framework of the nanocomposite.

previously reported rhombohedral SeO_2-based structures, suggesting the incorporation of CuO within the SeO_2 matrix.[40] The volume of a unit cell (289.49×10^6 pm^3) and the calculated density (5.23 g cm^{-3}) are also in good agreement with the reported values for pure SeO_2 minerals crystallized under high-temperature conditions.[40] For reference, standard CuO exhibits a monoclinic phase with lattice parameters $a = 4.683$ Å, $b = 3.425$ Å, $c = 5.128$ Å, $\beta = 99.5°$, confirming that the observed patterns correspond to the intended CuO/SeO_2 composite rather than pure CuO.

The diffraction peaks at $2\theta = 24.49°$, 33.59°, 36.19°, 39.75°, and 41.48° for the respective (012), (104), (110), (006), and (113) planes appeared with high intensities (up to 100%), corroborating the high crystallinity of the composite. They are typical reflections of SeO_2 and matched with the reference data (PDF 84-1616 and PDF 82-1465), hence confirming that the crystallographic framework did not collapse after the incorporation of CuO. Similarly, SeO_2 crystallinity was preserved for the biogenic Ag/SeO_2 nanomaterials prepared using plant extracts.[40] Table 1 compares lattice parameters, densities, and major 2θ peaks of the CuO/SeO_2 NC, the polysaccharide-functionalized NC, and standard references, confirming phase retention and lattice modifications.

The functionalization of CuO/SeO_2 with the polysaccharide matrix resulted in a significant shift in lattice parameters and peak positions of the CuO/SeO_2/polysaccharide NC. Its unit cell parameters reduced to $a = b = 4.7580$ Å and $c = 12.9910$ Å, while a significant cell volume reduction to 254.70×10^6 pm^3 along with a density reduction to 3.99 g cm^{-3} (calculated) and 4.05 g cm^{-3} (measured) was observed. These observations are characteristic of a lattice contraction, typically ascribed to (i) interfacial interactions between polysaccharide chains and metal–oxygen clusters, (ii) partial lattice strain induced by hydrogen bonding, and (iii) reduced long-range ordering due to polymeric encapsulation.[44–46] Analogous phenomena have been recorded in selenium–arabinogalactan nanocomposites[44] and

Table 1 Comparison of lattice parameters, unit cell volume, density, and prominent 2θ diffraction peak for CuO/SeO_2 NC, polysaccharide-functionalized CuO/SeO_2 NC, and standard reference materials. From this comparison, it is evident that lattice parameters decrease and diffraction peaks shift upon polysaccharide functionalization, while maintaining that SeO_2 possesses a crystal structure in CuO/SeO_2 NC and polysaccharide-functionalized CuO/SeO_2 NC. The unit cell volume decreases by 12% and the prominent diffraction peak shifts from 33.59° (104) to 35.14° (104) for polysaccharide-functionalized CuO/SeO_2 NC

Sample	Space group	Lattice parameters (Å)	Unit cell volume ($\times 10^6$ pm^3)	Density (g cm^{-3})	Major 2θ peaks (°) (planes)
CuO/SeO_2 NC	$R\bar{3}c$ (167)	$a = b = 4.9588$, $c = 13.5942$	289.49	5.23	24.49 (012), 33.59 (104), 36.19 (110), 39.75 (006), 41.48 (113)
CuO/SeO_2/ polysaccharide NC	$R\bar{3}c$ (167)	$a = b = 4.7580$, $c = 12.9910$	254.70	3.99 (calcd), 4.05 (measured)	25.58 (012), 35.14 (104), 37.79 (110), 41.22 (006), 42.10 (113)
Standard SeO_2	$R\bar{3}c$	$a = b = 4.955$, $c = 13.590$	288.8	5.25	24.45 (012), 33.55 (104), 36.15 (110), 39.70 (006), 41.45 (113)
Standard CuO	$C2/c$	$a = 4.683$, $b = 3.425$, $c = 5.128$, $\beta = 99.5°$	77.38	6.31	32.52 (110), 35.60 (002), 38.72 (111), 48.73 (202)

polysaccharide hydrogels loaded with Cu nanoparticles.[45] The most intense reflection shifted to (I = 90%) at $2\theta \approx 35.14°$ corresponding to the (104) plane in the polysaccharide-modified sample, replacing the dominant peak at 33.59° in the unmodified composite. The change in relative intensities indicates a preferred-orientation effect caused by the polymer network. Furthermore, some peaks showed a slight displacement at higher angles (*e.g.*, from 24.49° → 25.58°, 33.59° → 35.14°, 36.19° → 37.79°), indicating increased lattice strain, as characteristic of the formation of the organic–inorganic interface. Similar shifts have been reported for biogenic SeO_2 nanostructures, in which capping agents introduced a moderate compressive strain in the lattice.[40]

High crystallinity was still observed for CuO/SeO_2/polysaccharide NC, with sharp reflections at 52.55°, 57.52°, and 66.55° corresponding to (024), (116), and (214) planes, respectively; however, the FWHM of some selected peaks is somewhat broader compared with the pristine composite, indicating the decrease in crystallite size and increased surface disorder on polymer encapsulation. Using the Scherrer equation, the estimated crystallite size decreased from *ca.* 28 nm (uncoated) to *ca.* 22 nm (polysaccharide-coated), confirming the effect of polymer encapsulation on structural refinement. A similar trend has been observed for biopolymer-stabilized metal oxide systems such as alginate, pectin, and chitosan nanocomposites incorporating CuO or ZnO.[46] In general, the XRD results illustrate that polysaccharide coating does not disrupt the rhombohedral structure but instead induces changes in lattice dimensions, crystallinity, and preferred orientation. Such modifications reflect a strong chemical interaction between the polysaccharide matrix and the CuO/SeO_2 core, which was expected from previously reported polysaccharide-stabilized metal oxide nanomaterials.[44–46] Further structural stabilization, as noticed, also corroborates the improved colloidal stability and distribution of surface charge given from the zeta potential analyses. From the above XRD analysis, the results indicate that the CuO/SeO_2 core retains its rhombohedral phase and experiences lattice contraction and preferred orientation upon polysaccharide functionalization.

3.3. Phytochemical analyses

The phytochemical composition of clove extract and the synthesized CuO/SeO_2-based nanocomposites was quantitatively assessed in terms of total phenolics, flavonoids, tannins, and carbohydrates (Table S5 and Fig. 9a). Clove extract exhibited the highest phenolic content (312.2 ± 1.74 mg GAE per g), moderate flavonoid content (48.64 ± 0.19 mg CE per g), low tannin content (6.147 ± 0.41 mg TAE per g), and substantial carbohydrate levels (482.93 ± 1.97 mg GE per mL).

Upon green synthesis of CuO/SeO_2 NC, the phenolic content decreased to 225.4 ± 1.98 mg GAE per g, accompanied by a slight reduction in flavonoids (45.25 ± 0.08 mg CE per g) and a minor increase in tannins (6.705 ± 0.16 mg TAE per g), while carbohydrate content slightly decreased (431.22 ± 2.91 mg GE per mL). The decline in phenolic content likely reflects the consumption of polyphenols as reducing and stabilizing agents during nanoparticle formation, consistent with previous reports on green synthesis using plant extracts.[25,29] These bioactive molecules act as electron donors, reducing metal ions to form nanocomposites and capping the resulting particles to enhance stability.

Notably, in CuO/SeO_2/polysaccharide NCs, there was an additional reduction in phenolic compounds (206.8 ± 0.97 mg GAE per g) as well as a significant increase in flavonoids (72.32 ± 1.07 mg CE per g), tannins (8.096 ± 0.08 mg TAE per g), and carbohydrate content (686.34 ± 3.54 mg GE per mL). The additional presence of polysaccharides contributes to this increase; beyond serving as a carbohydrate component, they interact with flavonoids and tannins, leading to enhanced measured levels of these compounds. The polysaccharides can be viewed as capping agents that enhance dispersibility while also increasing or retaining specific amounts of bioactive agents in nanocomposites.[19] The combination in green-synthesized nanocomposites has been observed in other articles, whereby polysaccharide components can cover and increase retention of compounds such as those belonging to flavonoids, in addition to phenolic compounds, hence increasing their activity as antioxidant and functional agents.[19,25]

In general, phytochemical screenings indicate that phenolics are primarily consumed during nanoparticle preparations, although the polysaccharide layer may enhance the availability of flavonoids, tannins, and carbohydrates. These compositional shifts are critical, as they directly influence the antioxidant and biological activities of the nanocomposites, aligning with observations in previously reported green-synthesized metallic and metal oxide nanomaterials.[18,19,25,29]

3.4. Antioxidant activity

The antioxidant potential of clove extract and synthesized CuO/SeO_2-based nanocomposites was evaluated using DPPH radical scavenging, ferric reducing power (FRAP), and phosphomolybdate assays (Tables S6, S7 and Fig. 9b, c). These complementary methods allowed assessment of free radical scavenging, electron-donating capacity, and total reductive potential, providing a comprehensive evaluation of antioxidant efficacy.

3.4.1. DPPH radical scavenging. In the DPPH assay, all the tested samples were found to be concentration-dependent free radical scavengers. Clove extract exhibited strong free radical scavenging activity with an IC_{50} of 0.013 ± 0.002 mg mL^{-1}. CuO/SeO_2 NC exhibited comparable activity (IC_{50} = 0.0126 ± 0.008 mg mL^{-1}), whereas the CuO/SeO_2/polysaccharide NC showed the highest activity (IC_{50} = 0.0096 ± 0.001 mg mL^{-1}) (Fig. 9b and Table S6).

The high effectiveness of the polysaccharide-coated nanocomposite can be justified due to the stabilizing role of the sugar matrix that facilitates higher solubility as well as increased access to phenolic and flavonoid compounds to act as effective hydrogen or electron-donating agents in neutralizing the DPPH radicals.[25,29] Compared to ascorbic acid (IC_{50} = 0.022 ± 0.003 mg mL^{-1}), all investigated samples showed stronger

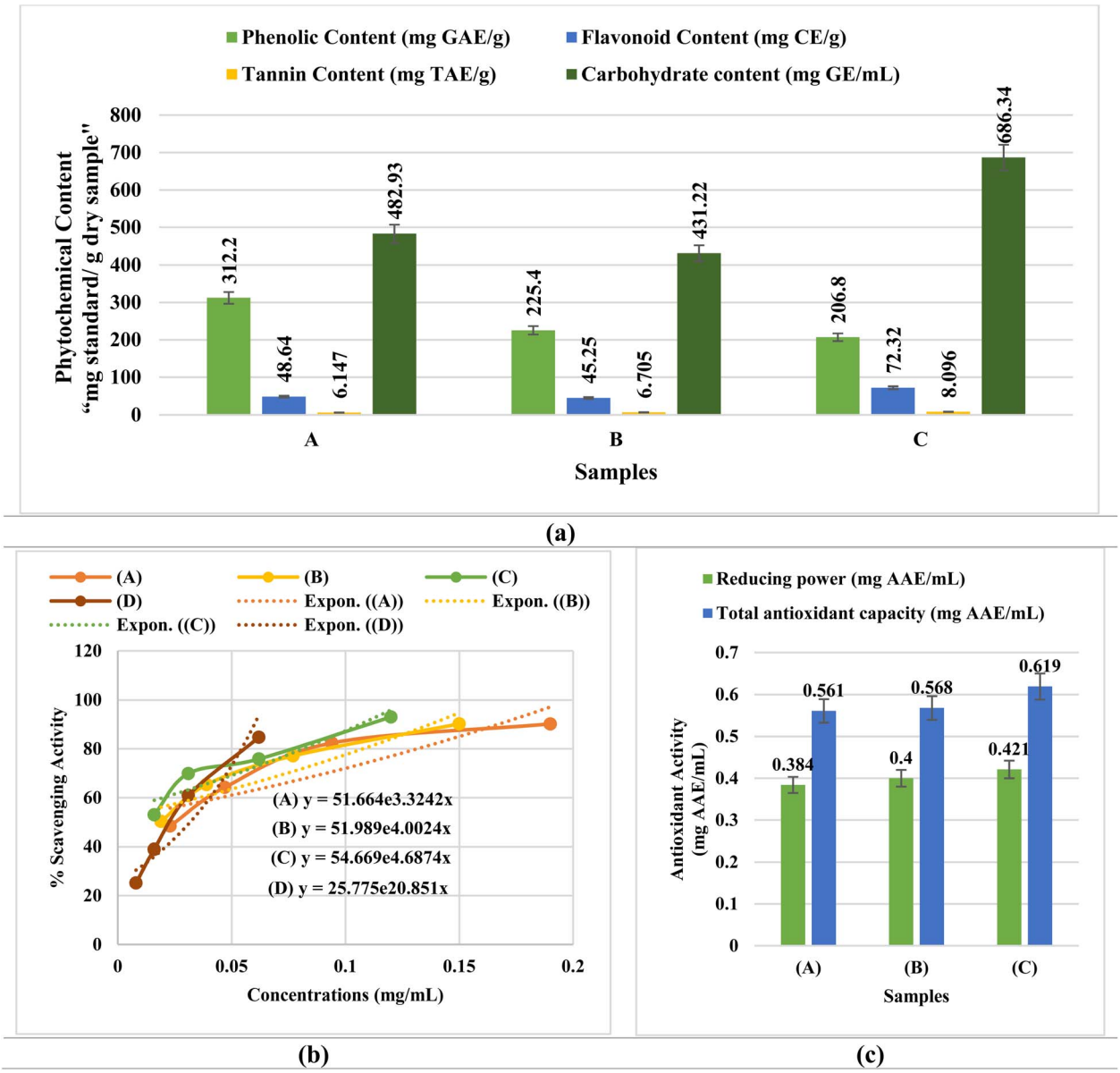

Fig. 9 Phytochemical analysis and antioxidant activity. (a) A comparison of the results of the phytochemical contents of the investigated samples. Clove (A); CuO/SeO_2 NC (B); CuO/SeO_2/polysaccharide NC (C). (b) The antioxidant results from the DPPH assay, the % scavenging activity plotted *versus* sample concentrations (mg mL^{-1}). Clove (A); CuO/SeO_2 NC (B); CuO/SeO_2/polysaccharide NC (C), and ascorbic acid (D). (c) Antioxidant activity of clove extract and nanocomposites evaluated by ferric reducing power and phosphomolybdate assays.

radical scavenging at similar concentrations, reflecting the high antioxidant density in both plant extract and nanocomposites.

3.4.2. Ferric reducing power and phosphomolybdate assays. In the FRAP assay, the reducing power was in the following order: CuO/SeO_2/polysaccharide NC (0.421 ± 0.16 mg AAE per mL) > CuO/SeO_2 NC (0.400 ± 0.08 mg AAE per mL) > clove extract (0.384 ± 0.10 mg AAE per mL). Similarly, the phosphomolybdate assay indicated that the total antioxidant capacity for the polysaccharide-coated nanocomposite was 0.619 ± 0.07 mg AAE per mL, 0.568 ± 0.05 mg AAE per mL for CuO/SeO_2 NC, and 0.561 ± 0.03 mg AAE per mL for clove (Fig. 9c and Table S7). These observations suggest an enhancement in electron-donation capacity and overall antioxidant potential upon polysaccharide coating, probably due to the stabilization of bioactive phytochemicals and facilitation in redox reactions.[18,25,47–51]

Although all three techniques demonstrated the potency of the polysaccharide-coated nanocomposite compared to the other two, variations in results can be attributed to the differences in mechanisms of action of each technique. The DPPH assay is based on the scavenging activity against free radicals through the donation of a hydrogen atom or an electron to the free radical. FRAP is based on the ability to reduce the ferric ion (Fe^{3+}) to ferrous ion (Fe^{2+}), and the phosphomolybdic acid assay estimates the overall reducing ability in acid environment.[49–51] Results, in all assays, were consistent and showed the following

order: CuO/SeO_2/polysaccharide NC > CuO/SeO_2 NC ≈ clove extract.

The antioxidant properties of clove and CuO/SeO_2 nanocomposites can be attributed mainly to their polyphenols and flavonoids. In the DPPH screening assay, these compounds can donate electrons or hydrogen atoms to interact with DPPH radicals and produce stable DPPH-H adducts, which lead to a reduction in levels of 517 nm absorbance.[52,53] Polyphenols and flavonoids donate electrons to reduce Fe^{3+} to Fe^{2+} in the FRAP assay, while in the phosphomolybdate assay, Mo(VI) can be reduced to Mo(V), producing a green phosphate–Mo(V) complex with 695 nm absorbance.[49,50] The polysaccharide layer may work synergistically by increasing electron donation and solubility and reducing redox molecule instability, thereby increasing their ability to scavenge radicals and act as reducing agents.[47,48]

In conclusion, the combined results reveal the enhanced antioxidant ability of the CuO/SeO_2/polysaccharide NC through every mechanism, and the results demonstrate the potential use of the material as a multi-functional antioxidant scaffold. The results are in agreement with the previously reported studies using plant-mediated and polysaccharide-stabilized nanocomposites.[25,29] However, it is worth mentioning that the antioxidant activities of both the CuO/SeO_2 NC and the CuO/SeO_2/polysaccharide NC were thoroughly investigated under the same experimental conditions (Tables S6 and S7). The improved antioxidant activity of the polysaccharide-functionalized nanocomposite compared to the unmodified CuO/SeO_2 NC may suggest the significant effect of surface modification on the enhancement of the scavenging activity and reducing power. Nevertheless, the lack of physical mixture control (the mixture of the CuO/SeO_2 NC and polysaccharide without surface modification) should be taken into account, and further investigations are required.

Comparative analysis of the activity of clove extract, CuO/SeO_2 NC, and CuO/SeO_2/polysaccharide NC reveals that the enhancement in the antioxidant activity is due to the combined effect of the synergy between the two metals and the surface modification effect of the second component in the NCs. The similar activity of clove extract and CuO/SeO_2 NC reveals that the additive effect alone cannot be the reason for the enhancement in the activity, while the further enhancement in the activity of CuO/SeO_2/polysaccharide NC reveals the effect of the dispersion of the active sites.

To further distinguish between synergistic and additive effects, future studies should include a physical mixture control (CuO/SeO_2 + polysaccharide without *in situ* functionalization). This would allow direct comparison and more rigorous confirmation of functionalization-induced enhancements.

3.5. Time-dependent release of Cu^{2+} and Se^{4+} ions

The Cu^{2+} and Se^{4+} ions release profile for CuO/SeO_2 NC and CuO/SeO_2/polysaccharide NC was also studied in Mueller–Hinton broth at 37 °C for 48 h. The results are shown in Table S8. From the results obtained for the bare CuO/SeO_2 NC, it is clear that the concentration of ions increases with time. However, while the concentration of Cu^{2+} ions increases from 1.12 ± 0.05 μg mL^{-1} to 6.75 ± 0.20 μg mL^{-1} after 48 h, the concentration of Se^{4+} ions also increases from 0.48 ± 0.02 μg mL^{-1} to 3.82 ± 0.11 μg mL^{-1}. This shows that the bare nanocomposite is capable of releasing ions into the environment. This behavior likely contributes to its broad-spectrum antibacterial activity. However, for the polysaccharide-functionalized CuO/SeO_2 NC, the ions are released much more slowly. In this case, only 3.42 ± 0.14 μg mL^{-1} and 2.05 ± 0.07 μg mL^{-1} of Cu^{2+} and Se^{4+} ions, respectively, were released after 48 h. This could be due to the stabilizing effect of the polysaccharide that acts as a barrier for the ions. The slower rate of ion release is consistent with the strain-dependent antibacterial performance of the polysaccharide-coated NC, wherein the antibacterial activity of the NC against certain Gram-positive bacteria increased, whereas the antibacterial activity of the NC against certain Gram-negative bacteria was slightly diminished. The ICP-MS results have further emphasized that the polysaccharide coating effectively provides a controlled release of Cu^{2+} and Se^{4+} ions to enhance the stability of the nanoparticles and fine-tune the antibacterial behavior. The slower kinetics also imply that cytotoxicity and antibacterial activity can be reduced in real-life applications. This has demonstrated the ability of the polysaccharide coating to act as a stabilizer and a fine-tuner for the nanoparticles.

The comparative release profiles of ions for CuO/SeO_2 NC and CuO/SeO_2/polysaccharide NC again confirm that the observed biological activities are not only due to the combined effect of Cu and Se species, but also that they are significantly dependent on the release characteristics that are imparted by surface functionalization.

3.6. Antibacterial activity

The antibacterial efficiency of clove extract, CuO/SeO_2 NC, and CuO/SeO_2/polysaccharide NC was estimated for eight Gram-positive and Gram-negative bacterial strains, and values for the inhibition zone are presented in Fig. 10 and Table S9. Clove extract exhibited moderate antibacterial activity, with inhibition zones ranging from 14 to 19 mm. CuO/SeO_2 NC showed significantly higher inhibition zones (15–38 mm) compared to clove extract in most tested strains ($p < 0.05$). Notably high inhibition was observed against *K. pneumoniae* (38 ± 0.08 mm) and *E. cloacae* (37 ± 0.18 mm). CuO/SeO_2/polysaccharide NC exhibited strain-dependent antibacterial activity, with statistically significant differences observed between Gram-positive and Gram-negative strains ($p < 0.05$). The results of CuO/SeO_2/polysaccharide NC against *S. epidermidis* revealed an inhibition zone at 27 ± 0.52 mm, while low activities were observed against *K. pneumoniae* at 16 ± 0.60 mm and *E. cloacae* at 15 ± 1.53 mm. Statistical analysis using one-way ANOVA followed by Tukey's *post hoc* test confirmed that the differences in inhibition zone diameters among the tested samples were statistically significant ($p < 0.05$) for most bacterial strains (Table S9).

The addition of polysaccharide clearly affected the antibacterial activity of the nanocomposite. A comparison between CuO/SeO_2 NC and CuO/SeO_2/polysaccharide NC shows that the antibacterial activities cannot be merely contributed to the

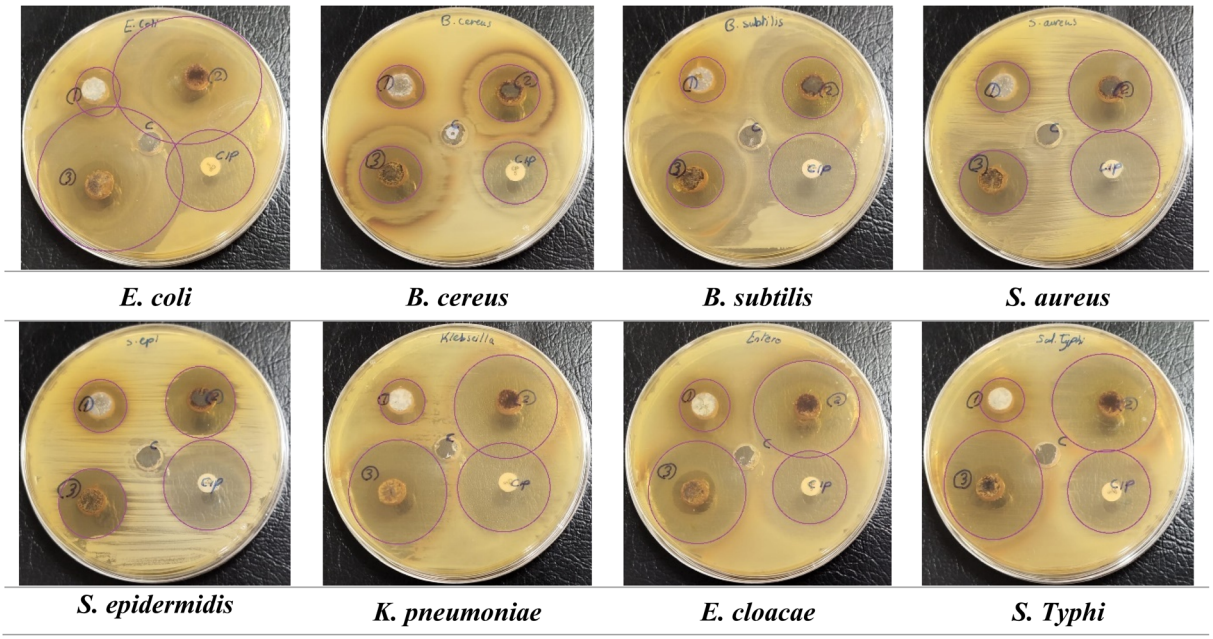

Fig. 10 Representative Petri dish images illustrating the antibacterial activity of clove extract (1), CuO/SeO_2 NC (2), and CuO/SeO_2/polysaccharide NC (3) against various pathogenic bacterial strains. The clear zones surrounding each sample indicate the inhibition of bacterial growth. Ciprofloxacin (5 μg) (Cip) was used as a positive control, and the control (C) (untreated) showed no inhibition.

additive effect of individual components. On the contrary, both the bimetallic synergistic effect and the surface functionalization-induced modulation are involved. However, the general activity of CuO/SeO_2/polysaccharide NC was not higher compared with the uncapped NC, although its interactions with different bacterial strains were affected by the biopolymer coating. This led to enhanced activity against Gram-positive bacterial strains and a reduction in effectiveness against Gram-negative bacterial strains. Although the overall antibacterial effect was lower in some Gram-negative bacteria, the polysaccharide coating facilitated ion release and selective activity, which may lessen cytotoxicity and enable targeted antimicrobial therapy. Since such strain-specific behavior may be indicative of the regulatory role of a polysaccharide layer concerning surface exposure, ion release, and microbial interactions to enable selective rather than broad-spectrum enhancements, it has been concluded that the polysaccharide capping is a versatile method for fine-tuning the biological performance of nanocomposites by enhancing their stability and guiding antimicrobial activity toward target bacterial strains.

The antibacterial activity observed for the CuO/SeO_2 NC agrees with literature reports on the effective antimicrobial activity of copper–selenium systems. Alavi and Kennedy[54] reported that plant-based CuO and ZnO nanostructures exhibited superior antibacterial activity because of their affinity to interact and destabilize microbial membranes. In addition, Abou Baker and Abbas[55] reported that CuO/Se nanocomposites inhibited *Helicobacter pylori* through combined ion release and oxidative stress mechanisms, which further substantiates the superior performance of our CuO/SeO_2 NC, especially against Gram-negative strains. Furthermore, the high inhibition zones recorded in this study surpass those biosynthesized SeO_2 nanoparticles from *Hibiscus sabdariffa*, which are generally in the range between 10 and 18 mm,[38] and prove that the incorporation of CuO significantly enhanced the antimicrobial potential.

Such a variable response of the CuO/SeO_2/polysaccharide NC can be explained through the role of polysaccharide capping on the issue of nanoparticle–cell interaction. Polysaccharides themselves have been known to take part in antibacterial action by interfering with metabolic pathways and causing membrane depolarization, as was illustrated for *Cordyceps cicadae* polysaccharides.[56] This is manifested in our study as increased activity against *S. epidermidis*. Comparable results were also obtained in the work of Alamri,[37] where green-synthesized CuO/SeO_2 NC was characterized by broad-spectrum antibacterial action, superior to traditional metal oxide systems by virtue of synergistic nanoscale interactions. The inhibition zones measured in our study for *K. pneumoniae* and *E. cloacae* are comparable to those of ciprofloxacin for certain strains, highlighting the encouraging antimicrobial potential of the CuO/SeO_2 NC.

The sharp antibacterial activity of CuO/SeO_2 and CuO/SeO_2/polysaccharide NCs could be explained by a multistage mechanism involving different steps of physicochemical and biochemical interactions at the bacterial cell surface. Firstly, nanoscale CuO and SeO_2 particles may interact with negatively charged bacterial membranes, provoking their physical destruction and increasing permeability. This initial contact promotes the intracellular release of Cu^{2+} and Se^{4+} ions, which disturb enzymatic function, ribosomal activity, and induce protein misfolding. These ions may contribute to antimicrobial activity by interacting with thiol groups of protein and nucleic

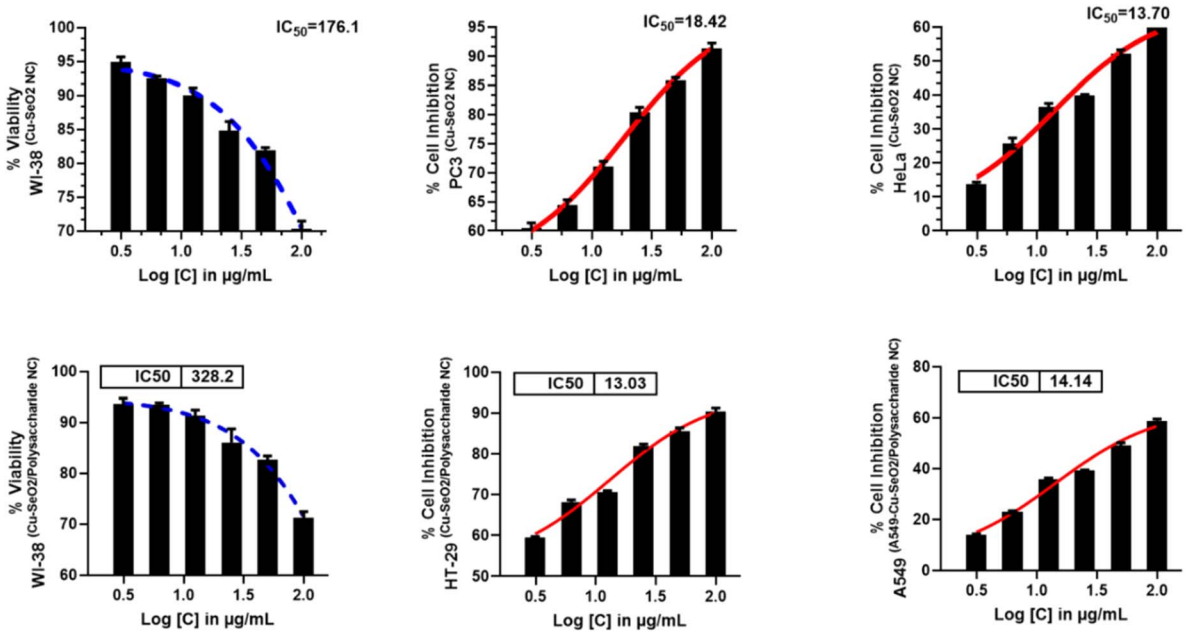

Fig. 11 MTT cytotoxicity responses of both unmodified Cu/SeO_2 nanocomposites and the polysaccharide-functionalized Cu/SeO_2/polysaccharide nanocomposites across normal and cancer cell lines. In the upper panel, WI-38 normal human lung fibroblasts are seen to maintain relatively high viability, while the PC3 prostate cancer cells and HeLa cervical cancer cells exhibit a clear dose-dependent increase in growth inhibition following exposure to Cu/SeO_2. The lower panel illustrates the biological activity of the polysaccharide-modified formulation, with WI-38 cells again displaying limited susceptibility, but HT-29 colorectal adenocarcinoma cells and A549 lung adenocarcinoma cells showing markedly enhanced sensitivity. The general trend of these findings is that cancerous cells (PC3, HeLa, HT-29, and A549) are more responsive to treatment compared with normal fibroblasts, and that polysaccharide functionalization enhances the antiproliferative potency of Cu/SeO_2 nanocomposites.

acid structures, thus interrupting critical cellular processes. Additionally, the measured release of ions from polysaccharide-capped NCs guarantees sustained antibacterial activity without sudden spikes in toxicity.

The better catalytic performance of CuO/SeO_2 NC than that of clove extract also confirms the bimetallic synergy between CuO and SeO_2 phases. Moreover, the changed catalytic properties of the polysaccharide-functionalized NC reveal the importance of surface modification in tuning catalytic properties rather than merely improving catalytic performance *via* additive effects. Besides this, both copper- and selenium-based nanomaterials are well-known generators of reactive oxygen species (ROS), including hydroxyl radicals and superoxide ions. Overproduction of ROS may result in lipid peroxidation, DNA fragmentation, and oxidative stress-mediated cell death, as was extensively described for metal–selenium nanostructures.[37,54] In a polysaccharide-capped nanocomposite, the biopolymer matrix enhances stability and dispersion and probably promotes controlled ion release, while the polysaccharide itself may act to impair nutrient uptake and interfere with cellular respiration.[56] Such synergy of ROS generation, ion toxicity, and membrane disruption provides a comprehensive explanation for the strong antibacterial effects observed in this study. ROS-induced oxidative stress has been widely documented to be one of the key mechanisms behind the antimicrobial and anticancer activities of CuO and selenium-based nanoparticles. Recent studies have further highlighted the therapeutic relevance of copper-mediated cell death pathways, including cuproptosis and cuproptosis-like mechanisms, in combating bacterial infections through disruption of microbial metabolic processes and oxidative homeostasis, as discussed by Wang *et al.*[57] However, ROS generation was not experimentally verified in this study. Hence, it is suggested that the involvement of ROS-induced oxidative stress can be regarded as one of the proposed mechanisms based on the literature. It should be noted that future studies using ROS-detecting probes in living cells (such as DCFH-DA-based fluorescence assays) are needed to confirm the involvement of ROS-induced oxidative stress in the observed activities.

While experiments have been carried out *in vitro* for ion release and antioxidant potential, the production of ROS and cell–nanoparticle interactions were not evaluated; hence, the suggested antimicrobial mode of action involving ROS-induced oxidative stress, membrane interaction, and ion-based toxicity is only from published research and needs additional experiments for its verification. Moreover, no animal-based studies have been conducted; therefore, the effectiveness of nanoparticles and their antibacterial mechanisms of action are only based on *in vitro* experiments and literature review. The antimicrobial effect is assumed to be due to the synergy effect caused by the breakdown of the bacterial cell wall, Cu^{2+} and Se^{4+} ion releases, and oxidative stress pathway mechanisms; however, there is a need for *in vivo* experiments that use proper infection models and include ROS measurement for validation purposes. Additionally, there are some limitations to be considered, such as the lack of direct ROS measurements,

Table 2 IC_{50} values and Selectivity Index (SI) of CuO/SeO_2 and CuO/SeO_2/polysaccharide nanocomposites[a]

Sample	Cell line	IC_{50} (μg mL^{-1})	SI (IC_{50} normal/IC_{50} cancer)
CuO/SeO_2 NC	WI-38 (normal)	176.1	—
	PC3	18.42	9.56
	HeLa	13.70	12.85
CuO/SeO_2/polysaccharide NC	WI-38 (normal)	328.2	—
	HT-29	13.03	25.19
	A549	14.14	23.21

[a] The Selectivity Index (SI) was calculated as SI = IC_{50} (normal cells)/IC_{50} (cancer cells). Interpretation of SI values: <1 = non-selective toxicity; 1–2 = weak selectivity; 2–10 = good selectivity; >10 = highly selective anticancer activity.

cellular uptake studies, and minimum inhibitory concentration/minimum bactericidal concentration tests, among others. These limitations should be addressed in order to provide more information about the functional interpretation proposed.

3.7. Anticancer activity

MTT assay results demonstrated clear concentration-dependent cytotoxicity of both Cu/SeO_2 and Cu/SeO_2/polysaccharide nanocomposites across all tested cell lines (Fig. 11). In normal WI-38 fibroblasts, treatment caused a gradual decrease in cell viability, with Cu/SeO_2 NCs exhibiting an IC_{50} of 176.1 μg mL^{-1}, whereas the Cu/SeO_2/polysaccharide formulation showed even lower toxicity (IC_{50} = 328.2 μg mL^{-1}), confirming their relative biocompatibility toward non-cancerous cells. In contrast, cancer cell lines showed markedly higher sensitivity. PC3 prostate cancer cells displayed strong dose-dependent growth inhibition, achieving an IC_{50} of 18.42 μg mL^{-1}, while HeLa cervical cancer cells also exhibited substantial susceptibility, with an IC_{50} of 13.70 μg mL^{-1} following Cu/SeO_2 NC treatment. For the polysaccharide-stabilized formulation, potent anticancer activity was again evident, with HT-29 colorectal cancer cells showing an IC_{50} of 13.03 μg mL^{-1} and A549 lung cancer cells exhibiting an IC_{50} of 14.14 μg mL^{-1}. The overall data indicate that both nanocomposite formulations selectively inhibit the growth of cancerous cells far more efficiently than normal cells, with polysaccharide functionalization enhancing safety while maintaining strong anticancer potency.

Our cytotoxicity results are in good agreement with previously reported studies on Cu/SeO_2-based nanocomposites and other selenium- or metal-based nanostructures.[58–60] Similar to Ahmed *et al.*[58] and Yu *et al.*,[59] our nanocomposites demonstrated remarkable dose-dependent cancer cell growth inhibition and relatively low toxicity toward normal fibroblasts, indicating a selective anticancer effect. In particular, the IC_{50} values for the cancer cell lines in our study were comparable or slightly lower compared with the IC_{50} values for polysaccharide-functionalized Cu/SeO_2 NCs, indicating that our formulation exerts potent antiproliferative effects through preserved biocompatibility. Finally, in accordance with Elmetwalli *et al.*[22] and Elmorsy *et al.*,[60] the increased cytotoxicity against prostate, cervical, colorectal, and lung cancers suggests that the nanocomposite architecture and surface functionalization contribute to a cell-type-specific uptake and activity that underpins the therapeutic relevance of these nanomaterials.

The cytotoxicity observed against our nanocomposites most likely results from the synergistic interplay between the induction of oxidative stress, modulation of intracellular redox, and mitochondrial dysfunction. Both copper and selenium components are known to generate reactive oxygen species (ROS) capable of damaging nucleic acids, proteins, and lipids, thereby triggering apoptotic pathways.[58] Selenium or SeO_2 moieties may modulate cellular redox states, augment ROS accumulation selectively in cancer cells, and disturb mitochondrial membrane potential to activate caspases and induce apoptosis.[58,60] Surface functionalization, such as polysaccharide or chitosan coating, may further enhance cellular uptake in malignant cells while reducing off-target effects in normal fibroblasts, contributing to both efficacy and safety of the nanocomposite formulation.

To quantitatively assess the therapeutic selectivity of the synthesized nanocomposites, the selectivity index (SI) was calculated using the IC_{50} values for normal WI-38 fibroblasts and cancer cell lines (Table 2). In this context, the CuO/SeO_2 nanocomposites exhibited selectivity indices of 9.56 for PC3 cells and 12.85 for HeLa cells. However, it is quite interesting to note that the polysaccharide-functionalized CuO/SeO_2 nanocomposites possess a higher selectivity index of 25.19 for HT-29 cells and 23.21 for A549 cells. Although the present study has clearly shown high selectivity toward multiple cancer cell lines compared to WI-38 human normal fibroblasts, further evaluation of the biosafety profile of the synthesized nanocomposites is necessary with other human cell types.

Although promising outcomes were achieved, certain aspects should be considered, such as the lack of physical mixture control, no actual ROS measurement, and the lack of *in vivo* testing. These factors must be taken into account in future experiments to better understand the application of these nanocomposites.

4 Conclusion

In the present work, a green synthesis method was successfully established for the preparation of CuO/SeO_2 nanocomposites and their polysaccharide-functionalized derivatives using a natural reducing agent derived from the extract of clove. The results revealed that the phytochemical-mediated redox reaction and the control of nucleation were helpful in the formation

of a CuO/SeO_2 core with strong Cu–O–Se bonding sites. The subsequent synthesis stage led to the formation of a core–shell-like structure due to polysaccharide adsorption without any interference with the Cu^{2+} and Se^{4+} ions. The outcomes clearly proved that there is high crystallinity, the same composition of elements, and encapsulation of the polymers. The functionalization of the polysaccharides resulted in lattice strain, reduced the size of the crystallites, and improved the colloidal stability remarkably, as evidenced by the highly negative zeta potential of −139.8 mV. The optical characterization results confirmed the increased absorption of visible light and low band gap energies, thus highlighting the improved electronic configuration and charge transfer capability. Phytochemical characterization confirmed the effective utilization of the phenolic compounds for the preparation of the nanocomposites, while the polysaccharides increased the availability of the flavonoids, tannins, and carbohydrates.

Functionally, the polysaccharide-coated nanocomposite exhibited superior antioxidant performance across several antioxidant assays with a DPPH IC_{50} of 0.0096 mg mL^{-1} and enhanced reducing power. Antibacterial studies showed strong and strain-dependent activity where the pristine CuO/SeO_2 NC was outstanding for Gram-negative bacteria, while polysaccharide coating enabled selective modulation of antibacterial efficacy toward Gram-positive strains. Importantly, cytotoxicity assessments showed that there was marked selectivity to cancer cells, while IC_{50} values as low as 13–18 μg mL^{-1} were recorded across multiple cancer lines; it showed very low toxicity against normal fibroblasts, confirming improved biocompatibility by polysaccharide functionalization.

Finally, this study demonstrates the potential of polysaccharide-functionalized CuO/SeO_2 nanocomposites as multifunctional nanomaterials, exhibiting significant *in vitro* biological activity and synthesized *via* a green-assisted technique. Although the synthesis employs plant-based reducing agents and mild conditions, a full quantitative assessment of its environmental footprint (*e.g.*, *E*-factor or life-cycle analysis) was not conducted in this study. The combination of green-assisted synthesis, enhanced physicochemical properties, and improved biological performance highlights promising *in vitro* applications of the synthesized nanocomposites as antioxidants, antibacterials, and anticancer agents. However, it is essential to note that all obtained data are based on *in vitro* experiments alone; further *in vivo* investigations are required to validate their biomedical applications.

Conflicts of interest

The authors declare that they have no known competing financial interests.

Data availability

The data supporting the findings of this study are available within the article and its supplementary information (SI). Supplementary information: detailed experimental procedures and extended results that support the main manuscript. Section S1 describes the materials, reagents, and analytical instruments used in the study, while Section S2 presents comprehensive SI results. These include FTIR vibrational band assignments for the clove extract and nanocomposites (Table S1), elemental composition determined by EDX analysis (Table S2), the results of XRD analyses (Tables S3 and S4), phytochemical contents of the investigated samples (Table S5), antioxidant activity evaluated by the DPPH assay with IC_{50} determination (Table S6), ferric reducing power and total antioxidant capacity results (Table S7), time-dependent release of Cu^{2+} and Se^{4+} ions (Table S8), and antibacterial activity against representative Gram-positive and Gram-negative bacterial strains (Table S9). Concisely, these SI tables provide additional validation of the synthesis, surface functionalization, and biological performance of the prepared nanocomposites, ensuring data transparency and reproducibility. See DOI: https://doi.org/10.1039/d6ra00556j.

Acknowledgements

This work is supported by the Ongoing Research Funding Program (ORF-2026-505), King Saud University, Riyadh, Saudi Arabia.

References

1 Y. Cao, H. A. Dhahad, M. A. El Shorbagy and H. Q. Alijani, *Sci. Rep.*, 2021, **11**, 23479.
2 M. Sun, T. Wang, L. Li, X. Li, Y. Zhai and Y. Zhang, *Front. Pharmacol.*, 2021, **12**, 752445.
3 E. O. Mikhailova, *Molecules*, 2023, **28**, 8125.
4 S. Dhingra, N. A. A. Rahman, E. Peile, M. Rahman and M. Sartelli, *Front. Public Health*, 2020, **8**, 535668.
5 G. V. Vimbela, S. M. Ngo, C. Fraze, L. Yang and D. A. Stout, *Int. J. Nanomed.*, 2017, **12**, 3941–3965, DOI: 10.2147/IJN.S134526.
6 C. Cao, M. Abbasi, H. Q. Alijani, M. R. Akbarizadeh, S. Iravani, M. Barani, K. Najafi, S. Khatami and M. Khatami, *Ceram. Int.*, 2022, **48**, 3448–3454.
7 M. Haghighat, H. Q. Alijani, M. Ghasemi, S. Khosravi, F. Borhani, F. Sharifi, S. Iravani, K. Najafi and M. Khatami, *Bioproc. Biosyst. Eng.*, 2022, **45**, 97–105.
8 K. P. Trayes and S. E. Cokenakes, *Am. Fam. Physician*, 2021, **104**, 171–178.
9 M. Barani, M. Mukhtar, A. Rahdar, G. Sargazi, A. Thysiadou and G. Z. Kyzas, *Molecules*, 2021, **26**, 186.
10 H. Steinbrenner, B. Speckmann and L.-O. Klotz, *Arch. Biochem. Biophys.*, 2016, **595**, 113–119.
11 J. E. Abo Neima, A. A. Ahmed, M. El Sheekh and M. E. M. Makhlof, *Front. Mol. Biosci.*, 2023, **10**, 1120422.
12 A. Sentkowska and K. Pyrzyńska, *Appl. Sci.*, 2023, **13**, 1071.
13 F. Martínez Esquivas, J. M. Guzmán-Flores and A. Pérez-Larios, *Part. Sci. Technol.*, 2022, **41**, 319–329.
14 G. F. Aaga and S. T. Anshebo, *Heliyon*, 2023, **9**, e16067.
15 A. Lomelí Marroquín, *Int. J. Nanomed.*, 2019, **14**, 2171–2187.
16 R. Rasheed, A. Bhat, B. Singh and F. Tian, *Biomedicines*, 2024, **12**, 994.

17 B. Tepsongkroh, C. Thaihuttakij, S. Supawong and K. Jangchud, *Food Chem.: X*, 2023, **19**, 100864.
18 K. M. Elattar, N. M. Askar, N. H. Elhusseini, D. A. Omar, A. S. Ashry, M. M. Keshk, T. R. Saad, A. M. Elzeghiby, A. H. Elnakadi, M. Y. Aboelfatoh and M. Abdelaal, *ChemistrySelect*, 2025, **10**, e03394.
19 A. A. Alanazi, W. I. Saber, M. A. AlDamen and K. M. Elattar, *Int. J. Biol. Macromol.*, 2024, **280**, 135862.
20 N. M. Eldadamony, A. A. Ghoniem, A. A. Al-Askar, A. A. Attia, M. S. El-Hersh, K. M. Elattar, H. Alrdahi and W. I. Saber, *Int. J. Biol. Macromol.*, 2024, **269**, 132109.
21 A. A. Alanazi, W. I. Saber, M. A. AlDamen and K. M. Elattar, *Int. J. Biol. Macromol.*, 2025, **308**, 142533.
22 A. Elmetwalli, S. Abdelsayed, A. Elsayed, M. S. El-Hersh, M. G. Hassan, L. A. Gad, M. A. Salah, M. B. Y. Basiouny, M. A. Shaheen, M. F. Ibrahim, A. M. Ibrahim, H. M. Newish, E. Alhomaidi, A. H. El-Far and K. M. Elattar, *Med. Oncol.*, 2025, **42**, 414.
23 K. Zhang, M. Gao, G. Zheng, P. Xu, Y. Fu, L. Qiu, F. Yu, Y. Shen, M. Wang, X. Hu and Y. Sun, *Int. Dent. J.*, 2025, **75**, 1420–1430.
24 (*a*) K. M. Elattar, M. S. El Hersh, G. Bonanomi, A. M. Abd-ElGawad, Y. A. El-Amier and A. A. Al-Huqail, *RSC Adv.*, 2025, **15**, 39336–39354; (*b*) M. M. Alsowayigh, A. H. Alsehli, F. Alqahtani, F. Abdulaziz, M. Tounsi, H. Bin Bosayes, A. Alanazi and K. M. Elattar, *Int. J. Environ. Sci. Technol.*, 2026, **23**, 163.
25 (*a*) K. M. Elattar, A. A. Ghoniem, F. O. Al-Otibi, A. S. Fakhouri, Y. A. Helmy, W. I. Saber, M. A. Hassan and A. Elsayed, *RSC Adv.*, 2025, **15**, 12100–12116; (*b*) M. Abdelaal, J. H. Elebeidy, N. S. El-Gendi, H. O. Taha, W. A. Ahmed, O. S. E.-D. M. S. El-Din Marghny, R. N. Rezk, L. H. Abdelaal, A. S. Elmenshawy and K. M. Elattar, *J. Water Process Eng.*, 2026, **82**, 109423.
26 M. R. M. Askar, *RSC Adv.*, 2025, **15**, 13152–13171.
27 (*a*) A. A. Alanazi, K. M. Elattar, F. Abdulaziz and M. M. Hammouda, *Int. J. Biol. Macromol.*, 2026, **353**, 151300; (*b*) A. A. Alanazi, K. M. Elattar, F. Abdulaziz and M. M. Hammouda, *Int. J. Biol. Macromol.*, 2026, **352**, 151032.
28 M. G. Hassan, H. S. Farouk, D. M. Baraka, M. Khedr and A. Elmetwalli, *Inorg. Chem. Commun.*, 2024, **168**, 112853.
29 K. M. Elattar, A. Elmetwalli, O. R. Alzahrani, A. A. Ghoniem, M. G. Hassan, S. Abdelsayed, A. A. Zaher, D. K. Sabir and A. Elsayed, *Med. Oncol.*, 2025, **42**, 339.
30 A. Elmetwalli, M. O. Abdel-Monem and A. H. El-Far, *Med. Oncol.*, 2024, **41**, 106.
31 S. Poulston, P. M. Parlett, P. Stone and M. Bowker, *Surf. Interface Anal.*, 1996, **24**, 811–820.
32 R. Würz, A. Meeder, D. Fuertes Marron, T. Schedel-Niedrig, A. Knop-Gericke and K. Lips, *Phys. Rev. B: Condens. Matter Mater. Phys.*, 2004, **70**, 205321.
33 G. N. K. Reddy, A. V. Sekhar, L. Pavić, A. Bafti, J. Pisk, A. S. S. Reddy, N. Venkatramaiah, G. N. Raju, V. R. Kumar and N. Veeraiah, *Appl. Phys. A*, 2023, **129**, 208.
34 S. Kesavan, D. Rajesh, J. Shanmugam, S. Aruna, M. Gopal and S. Vijayakumar, *Int. J. Biol. Macromol.*, 2023, **244**, 125322.
35 K. Syrek, M. Zych, M. Pisarek, Ł. Gondek, M. Gurgul, R. Palowska, L. Liu and G. D. Sulka, *J. Power Sources*, 2025, **640**, 236656.
36 X. Gao, X. Li, J. Mu, C. T. Ho, J. Su, Y. Zhang, X. Lin, Z. Chen, B. Li and Y. Xie, *Int. J. Biol. Macromol.*, 2020, **152**, 605–615.
37 F. B. Alamri, *J. Nanotechnol.*, 2025, **2025**, 1027481.
38 A. Bahari, S. I. Esmail and A. M. Alattar, *J. Med. Phys.*, 2024, **49**, 557–562.
39 X. Song, Y. Chen, H. Sun, X. Liu and X. Leng, *Carbohydr. Polym.*, 2021, **255**, 117379.
40 A. A. Ghoniem, K. M. Elattar, F. O. Al-Otibi, A. Elsayed, M. S. El-Hersh, A. Y. El-Khateeb, Y. A. Helmy and W. I. Saber, *RSC Adv.*, 2024, **14**, 7088–7111.
41 S. T. Zhang, W. X. Wen, P. P. Chen, S. C. Dong, H. Zhang, J. Z. Chen and D. L. Zhao, *Small*, 2025, **21**, e07592.
42 B. Boury and S. Plumejeau, *Green Chem.*, 2015, **17**, 72–88.
43 J. Ray, B. Mondal, R. K. Saren and T. Tripathy, *Bull. Mater. Sci.*, 2025, **48**, 21.
44 A. V. Papkina, A. I. Perfileva, M. A. Zhivet'yev, G. B. Borovskii, I. A. Graskova, I. V. Klimenkov, M. V. Lesnichaya, B. G. Sukhov and B. A. Trofimov, *Nanotechnol. Russ.*, 2015, **10**, 484–491.
45 J. F. Souza, G. P. Costa, R. Luque, D. Alves and A. R. Fajardo, *Catal. Sci. Technol.*, 2019, **9**, 136–145.
46 R. Y. Pastrana-Alta, E. Huarote-Garcia, M. A. Egusquiza-Huamani and A. M. Baena-Moncada, *RSC Adv.*, 2025, **15**, 35807–35843.
47 A. Kausar, *Polym.-Plast. Technol. Mater.*, 2023, **62**, 582–603.
48 S. O. Alzahrani, A. Alisaac, M. Alsahag, F. M. Aldosari, N. M. Alshammari, M. H. Alhalafi, A. O. Obaid and N. M. El-Metwaly, *Int. J. Biol. Macromol.*, 2025, 144220.
49 J. Hua, F. Wang, X. Wei, Y. Qin, J. Lian, J. Wu, P. Ma and X. Ma, *Int. J. Mol. Sci.*, 2023, **24**, 4317.
50 X. Bi and P. Westerhoff, *Environ. Sci.: Nano*, 2019, **6**, 1791–1798.
51 R. L. Vifta and F. P. Luhurningtyas, *Indones. J. Cancer Chemoprevent.*, 2020, **11**, 22–29.
52 W. Zhang, Z. Zeng and J. Wei, *J. Phys. Chem. C*, 2017, **121**, 18635–18642.
53 S. Baliyan, R. Mukherjee, A. Priyadarshini, A. Vibhuti, A. Gupta, R. P. Pandey and C. M. Chang, *Molecules*, 2022, **27**, 1326.
54 M. Alavi and J. F. Kennedy, *Cellulose*, 2021, **28**, 3297–3310.
55 D. H. Abou Baker and H. S. Abbas, *Arab. J. Chem.*, 2023, **16**, 105095.
56 Y. Zhang, Y. T. Wu, W. Zheng, X. X. Han, Y. H. Jiang, P. L. Hu, Z. X. Tang and L. E. Shi, *J. Funct. Foods*, 2017, **38**, 273–279.
57 W. Wang, H. Gui, X. Wei, H. Liu and X. Wang, *Adv. Mater.*, 2025, **37**(37), 2506119.
58 N. A. Ahmed, E. M. Abdelrazek and H. Salaheldin, *Int. J. Biol. Macromol.*, 2024, **283**, 137765.
59 X. Yu, X. Deng, W. Qian, X. Luo, Q. He and J. He, *Mater. Express*, 2021, **11**, 287–295.
60 B. K. Elmorsy, O. Elkhawaga, E. Tolba and Z. El-Khayat, *Mansoura J. Chem.*, 2025, **68**, 11–16.